Analyzing correlation functions with tesseral and Cartesian spherical harmonics

Pawel Danielewicz
Department of Physics and Astronomy, and National Superconducting Cyclotron Laboratory, Michigan State University, East Lansing, Michigan 48824, USA

Scott Pratt
Department of Physics and Astronomy, Michigan State University, East Lansing, Michigan 48824, USA
(Received 17 December 2006; published 19 March 2007)

The dependence of interparticle correlations on the orientation of particle relative momentum can yield unique information on the space-time features of emission in reactions with multiparticle final states. In the present paper, the benefits of a representation and analysis of the three-dimensional correlation information in terms of surface spherical harmonics is presented. The harmonics include the standard complex tesseral harmonics and the real Cartesian harmonics. Mathematical properties of the lesser known Cartesian harmonics are illuminated. The physical content of different angular harmonic components in a correlation is described. The resolving power of different final-state effects with regard to determining angular features of emission regions is investigated. The considered final-state effects include identity interference, strong interactions, and Coulomb interactions. The correlation analysis in terms of spherical harmonics is illustrated with the cases of Gaussian and blast-wave sources for proton-charged meson and baryon-baryon pairs.

DOI: 10.1103/PhysRevC.75.034907 PACS number(s): 25.75.Nq

I. INTRODUCTION

Measurements of low-relative-velocity correlations yield access to the size and shape of relative emission sources in reactions with multiparticle final states [1–4]. This information plays an especially important role in in heavy ion collisions. The duration of emission, which is linked to the nuclear equation of state, can be also inferred from those measurements. Perhaps the most startling finding that occurred during the first years of the BNL Relativistic Heavy Ion Collider (RHIC) program was the disagreement between the features of experimentally determined emission sources [5–7] and predictions of hydrodynamic models [8–11] incorporating an anticipated phase transition, which would yield a long emission duration. A long emission duration would have resulted in an elongated shape ($R_{\rm out}/R_{\rm side} \gg 1$ in the usual RHIC nomenclature) of the emission source for particles of a specific momentum. In the literature, the most exhaustively studied correlation has been that produced by interference for identical mesons. For pure interference, the correlation expressed as a function of the relative particle momentum is related to the relative emission source through a simple Fourier transformation, principally yielding direct access to the source shape. In the measured charged-meson correlations, the Coulomb effects competing with interference had been normally compensated for with cumbersome corrections. However, as we demonstrate, the correlations induced by the Coulomb and further by the strong interactions can also provide information on the source shapes. For any type of correlation, the analysis is facilitated by the use of spherical harmonics, either the standard complex tesseral harmonics or the real Cartesian harmonics [12]. The harmonics allow for a straightforward faithful representation of the three-dimensional correlation data, and also better facilitate isolating and focusing on specific physical properties of the source. Different source parametrizations will be employed for illustration of our discussions. For example, the $\ell = 2$ harmonic expansion coefficients, characterizing quadrupole deformation, provide information on the ratio of radii $R_{\rm out}/R_{\rm side}$ in the common Gaussian source representation.

The correlation associated with the final-state effects at low relative velocities within a subsystem of the particles a and b can be linked to a source function $\mathcal{S}$ through the relation

$$\frac{d^6N^{ab}/d^3p_a d^3p_b}{(dN^a d^3p_a)(dN^b d^3p_b)} = 1 + \mathcal{R}(\boldsymbol{P},\boldsymbol{q}) = \int d^3r |\phi^{(-)}(\boldsymbol{q},\boldsymbol{r})|^2 \mathcal{S}(\boldsymbol{P},\boldsymbol{r}). \quad (1)$$

Here, $\mathcal{R}(\boldsymbol{P},\boldsymbol{q})$ is the deviation of the left-hand side correlation function from unity, $\boldsymbol{P}$ is the total momentum of the pair, and $\boldsymbol{q}$ is the relative momentum measured in the two-particle rest frame. The factor $|\phi^{(-)}|^2$ represents the relative wave function squared, in the two-particle rest frame, with asymptotic condition imposed on the outgoing wave. The square of the wave function is averaged over spins. The function $\mathcal{S}(\boldsymbol{P},\boldsymbol{r})$ represents the probability density that the particles a and b, moving with the same velocity $\boldsymbol{V}$ corresponding to the total momentum $\boldsymbol{P}$, are emitted from the reacting system a distance $\boldsymbol{r}$ apart in their rest frame. Since at large $\boldsymbol{q}$, the emission in multiparticle final states becomes uncorrelated, i.e., $\mathcal{R} \to 0$ while $|\phi^{(-)}|^2$ averages to 1 as a function of $\boldsymbol{r}$, it follows that $\mathcal{S}$ is normalized to 1, $\int d^3r \mathcal{S}(\boldsymbol{P},\boldsymbol{r}) = 1$. A detailed derivation of Eq. (1) can be found in Ref. [13] (see also Ref. [14]).

The probability density of emission at the relative distance may be expressed in terms of single-particle probability

densities s:

$$\mathcal{S}(\boldsymbol{P},\boldsymbol{r}) = \frac{\int d^4x_a d^4x_b s_a(m_a\boldsymbol{P}/(m_a+m_b),x_a) s_b(m_b\boldsymbol{P}/(m_a+m_b),x_b)\delta(\boldsymbol{r}-\boldsymbol{r}_a-\boldsymbol{r}_b)}{\int d^4x_a d^4x_b s_a(m_a\boldsymbol{P}/(m_a+m_b),x_a) s_b(m_b\boldsymbol{P}/(m_a+m_b),x_b)}, \tag{2}$$

where $s_a(\boldsymbol{p},x)$ is the density for emitting particles of type a with momentum $\boldsymbol{p}$ from space-time point x. The spatial arguments are for the frame moving at the center-of-mass velocity $\boldsymbol{V}$. According to Eq. (1), the correlation data access the probability distribution in the relative rest-frame separation only. Information on emission duration can only be inferred from the influence of that duration on the relative spatial distribution [15–17]. Similarly, single-particle distributions s can be deduced only indirectly from data (1) because of the folding in Eq. (2) with an integration over the average particle position. For a set of investigated particles, the constraining of single-particle distributions may be enhanced by an analysis of correlations (1) of all possible particle pairs.

In the following, we concentrate on what might be directly determined from data, i.e., the determination of $\mathcal{S}(\boldsymbol{P},\boldsymbol{r})$ given measurement of $\mathcal{R}(\boldsymbol{P},\boldsymbol{q})$. Since each individual value of $\boldsymbol{P}$ nominally represents a different problem, we suppress the $\boldsymbol{P}$ arguments in the functions. As access to $\mathcal{S}$ is conditioned on any deviations of $|\phi|^2$ from unity, we subtract unity from both sides of Eq. (1) arriving at

$$\mathcal{R}(\boldsymbol{q}) = \int d^3r[|\phi^{(-)}(\boldsymbol{q},\boldsymbol{r})|^2-1]\mathcal{S}(\boldsymbol{r}) \equiv \int d^3r\mathcal{K}(\boldsymbol{q},\boldsymbol{r})\mathcal{S}(\boldsymbol{r}), \tag{3}$$

where we have utilized the normalization of $\mathcal{S}(\boldsymbol{P},\boldsymbol{r})$. Here, both $\boldsymbol{q}$ and $\boldsymbol{r}$ are evaluated in a frame where $\boldsymbol{P}=0$. It is seen that $\mathcal{R}$ is related to $\mathcal{S}$ through an integral transform where $|\phi^2(\boldsymbol{q},\boldsymbol{r})|^2-1$ plays the role of the kernel $\mathcal{K}$ of transformation. The determination of $\mathcal{S}(\boldsymbol{r})$ from $\mathcal{R}(\boldsymbol{q})$ amounts then to the inversion of the integral transform, often referred to as imaging [18–23].

Imaging has already been extensively performed for angle-averaged correlation functions, $\mathcal{R}(q)$, which can provide angle-averaged distributions $\mathcal{S}(r)$. It is the goal of this paper to describe how one might extract the angular information in $\mathcal{S}(\boldsymbol{r})$ by decomposing $\mathcal{R}(\boldsymbol{q})$ in terms of surface-spherical tesseral and Cartesian harmonics. A parallel effort, employing tesseral harmonics in the case of pure interference, is described in Ref. [24].

The wave function squared $|\phi(\boldsymbol{q},\boldsymbol{r})|^2$ depends, after summation over spins, only on the magnitudes of q and r and on the angle θ_{qr} between $\boldsymbol{q}$ and $\boldsymbol{r}$. Thus, the square is invariant under rotations. As a consequence, the coefficients of expansion in terms of spherical harmonics, for the correlation and source functions, are directly related to each other [21],

$$\mathcal{R}_{\ell m}(q) = 4\pi \int dr r^2 \mathcal{K}_\ell(q,r)\mathcal{S}_{\ell m}(r). \tag{4}$$

Here, the expansion coefficients and expansion for the correlation function are defined by the relations

$$\begin{aligned}\mathcal{R}(\boldsymbol{q}) &= \sqrt{4\pi}\sum_{\ell m}\mathcal{R}^*_{\ell m}(q)Y_{\ell m}(\Omega),\\ \mathcal{R}_{\ell m}(q) &\equiv \frac{1}{\sqrt{4\pi}}\int d\Omega_q Y_{\ell m}(\Omega)\mathcal{R}(\boldsymbol{q}),\end{aligned} \tag{5}$$

with analogous expressions for the source function. The partial kernel $\mathcal{K}_\ell$ encodes the information from the wave function, that is,

$$\mathcal{K}_\ell(q,r) \equiv \frac{1}{2}\int d\cos\theta_{qr}[|\phi^{(-)}(q,r,\cos\theta_{qr})|^2-1] \times P_\ell(\cos\theta_{qr}). \tag{6}$$

According to the above, an (ℓ,m) coefficient of the correlation function is tied to the coefficient of the source function with the same (ℓ,m). Thus, the source restoration can be reduced to a series of one-dimensional inversions of the integral transformations for individual (ℓ,m), employing kernels for specific ℓ. This sequence of one-dimensional inversions is computationally simpler than a single three-dimensional inversion. The angular resolution of data would determine how far the restoration can proceed in ℓ.

One problem with the above is the emergence of complex coefficients for the real-valued correlation and source functions, lacking direct geometric interpretation. The last issue is circumvented by introducing an alternate real-valued basis in the space of spherical angles, surface-spherical Cartesian harmonics $\mathcal{A}_{\vec{\ell}}(\Omega)$ [12,25,26].

Cartesian harmonics $\mathcal{A}_{\vec{\ell}}$ are linear combinations of $Y_{\ell m}$ with different m but the same $\ell=\ell_x+\ell_y+\ell_z$. In terms of the directional unit vector $\boldsymbol{n}$ pointing in the Ω direction, the Cartesian harmonics are explicitly given by [12]

$$\begin{aligned}\mathcal{A}_{\vec{\ell}}(\Omega) = \sum_{\substack{\vec{m}\\ 0\leqslant m_i\leqslant \ell_i/2}}\left(-\frac{1}{2}\right)^m \frac{(2\ell-2m-1)!!}{(2\ell-1)!!}\frac{\ell_x!}{(\ell_x-2m_x)!m_x!}\\ \times\frac{\ell_y!}{(\ell_y-2m_y)!m_y!}\frac{\ell_z!}{(\ell_z-2m_z)!m_z!}\\ \times n_x^{\ell_x-2m_x}n_y^{\ell_y-2m_y}n_z^{\ell_z-2m_z},\end{aligned} \tag{7}$$

where $m=m_x+m_y+m_z$ and $(-1)!!=1$. The leading term of $\mathcal{A}_{\vec{\ell}}$ is $n_x^{\ell_x}n_y^{\ell_y}n_z^{\ell_z}$, while the subsequent terms ensure that $r^\ell\mathcal{A}_{\vec{\ell}}$ satisfies the Laplace equation and, thus, is a combination of the $Y_{\ell m}$ of different m.

The expansion in terms of Cartesian harmonics are defined with the relations

$$\begin{aligned}\mathcal{R}(\boldsymbol{q}) &= \sum_{\vec{\ell}} \frac{\ell!}{\ell_x!\ell_y!\ell_z!}\mathcal{R}_{\vec{\ell}}\mathcal{A}_{\vec{\ell}}(\Omega_{\boldsymbol{q}}) \\ &= \sum_{\vec{\ell}} \frac{\ell!}{\ell_x!\ell_y!\ell_z!}\mathcal{R}_{\vec{\ell}}\hat{q}_x^{\ell_x}\hat{q}_y^{\ell_y}\hat{q}_z^{\ell_z},\end{aligned} \tag{8}$$

$$\mathcal{R}_{\vec{\ell}}(q) \equiv \frac{(2\ell+1)!!}{\ell!}\int \frac{d\Omega_q}{4\pi}\mathcal{A}_{\vec{\ell}}(\Omega_q)\mathcal{R}(\boldsymbol{q}). \tag{9}$$

In many situations the explicit form of $\mathcal{A}_{\vec{\ell}}$ is not needed. Just the existence of the Cartesian harmonics and their properties justify representing a function of the spherical angle in the second series in Eq. (8).

Since $\mathcal{A}_{\vec{\ell}}$ is a combination of $Y_{\ell m}$ with $\ell = \ell_x + \ell_y + \ell_z$, the coefficients of expansion in terms of Cartesian harmonics for the source and correlation function are related to each other in the same way as the coefficients of expansion in terms of tesseral harmonics in Eq. (4), that is,

$$\mathcal{R}_{\vec{\ell}}(q) = 4\pi\int dr r^2 \mathcal{K}_\ell(q,r)\mathcal{S}_{\vec{\ell}}(r). \tag{10}$$

In the next section, the structure of the kernel $\mathcal{K}_\ell$ in Eqs. (4) and (10) is investigated for the cases of pure identical-particle interference and for strong interactions and Coulomb interactions within a pair. We find that all three classes of final-state effects provide significant resolving power for different ℓ. Section III provides a detailed discussion of the properties of Cartesian harmonics. The subsequent section presents a discussion of the utility of higher ℓ moments and their relation to specific geometric features of the source. In particular, we show that the $\ell = 1$ moments can reveal an offset between the probability clouds for two different species, that the $\ell = 2$ moments can reveal the magnitude and orientation of axes in the ellipsoidal approximation for a source, while the $\ell = 3$ moments can reveal the "boomerang" nature of a source. In Sec. V, the cases of Gaussian and blast-wave sources are studied, as examples, in quantitative detail. In the final section, we summarize our results and discuss the prospects and challenges expected in analyses employing the harmonics.

II. CORRELATION KERNELS $\mathcal{K}_\ell$

The ability to extract source $\mathcal{S}$ anisotropies depends on the kernels $\mathcal{K}_\ell(q,r)$ defined in Eq. (6). Data on $\mathcal{R}$ are obtained at a certain resolution in q and suffer from errors. The theoretical relation (1) involves approximations [13,27], in assuming that the relative momentum q is small compared to the scales characterizing the rest of the system and in ignoring final-state effects other than those between the two studied particles moving slowly relative to each other. If the kernels $\mathcal{K}_\ell$ drop rapidly as ℓ increases for typical q values and for values of r characteristic to the source function, there will be no chance to determine details of the shape of $\mathcal{S}(\boldsymbol{r})$. In the following, we analyze the situation for different types of final-state interactions at different ℓ, q, and r.

In the process of source restoration, the values of $\mathcal{R}_{\vec{\ell}}$ would be known at discrete values of q. In parallel, the source $\mathcal{S}_{\vec{\ell}}(r)$ might be discretized in r or decomposed in some basis. The source restoration would then amount to the inversion of a matrix out of $\mathcal{K}_\ell(q,r)$, cf. [21,28]. An inability to extract source features might be signaled by the proximity of matrix eigenvalues to zero, resulting in an instability of the inversion. Such a situation could be encountered when extracting details of $\mathcal{S}_{\vec{\ell}}$ in an r region where $\mathcal{K}_\ell$ lacks resolving power. Practical experience in matrix-inversion strategy in analyzing data has been gained for $\ell = 0$ [18–23]. Importantly, this strategy has revealed non-Gaussian features in $\mathcal{S}_{\ell=0}(r)$, which were especially significant for proton sources in intermediate energy collisions. More common in the literature than the source discretization, has been a parametrization of the source which is then fit to $\mathcal{R}$. When parametrizing the source in three dimensions, the benefit regarding angular moments can be in understanding a systematic of the moments $\mathcal{R}_{\vec{\ell}}$ and $\mathcal{S}_{\vec{\ell}}$ as a function of $\vec{\ell}$. With regard to the fit strategy, the features of $\mathcal{K}_\ell(q,r)$ determine what parameters of $\mathcal{S}$ may be potentially constrained by data.

In the first subsection, we discuss kernels for the case of pure identity interference between spin-0 bosons. The two subsequent subsections are dedicated to the Coulomb and the strong interactions. Before launching into a detailed discussion of specific classes of interactions, we emphasize a general observation that a three-dimensional source $S_{\vec{\ell}}(r)$, expanded in a Taylor series around $\boldsymbol{r} = 0$, behaves as r^ℓ for small r. Consequently, there is not much to be discerned about the source at small r for $\ell \geqslant 1$, particularly for large ℓ, and the structure of $K_{\ell\geqslant 1}$ at small r will not be overly important. On the other hand, much could be learned about the angular structure of the source at large r. However, when the large-r region gets mapped onto small q, the ability to gain angular information becomes limited by the experimental resolution capabilities. Thus, in practice, the most important features of $\mathcal{K}_{\ell\geqslant 1}(q,r)$ are those at moderate q combined with moderate to high r. The naive expectation regarding strong interactions may be that when an s wave dominates the interaction, there is no possibility of discerning source shapes. We shall see that this is not the case.

A. Kernels for spin-0 boson identity interference

For noninteracting identical spin-0 bosons, the squared relative wave function is

$$|\phi(q,r,\cos\theta_{qr})|^2 = 1 + \cos(2qr\cos\theta_{qr}), \tag{11}$$

where the relative momentum convention is that $\boldsymbol{q}$ stands for the momentum of one of the particles in the center-of-mass frame. In this case, the three-dimensional transformation (3) becomes the cosine Fourier transform [23]. Since the cosine term in Eq. (11) may be represented as the real part of $\exp(2i\boldsymbol{q}\cdot\boldsymbol{r})$ and the latter may be expanded in Legendre polynomials and spherical Bessel functions, the $\mathcal{K}_\ell$ transformations (4) and (10), with Eq. (6), emerge as the spherical Bessel transforms (see also Ref. [24])

$$\mathcal{K}_\ell(q,r) = \begin{cases}(-1)^{\ell/2}j_\ell(2qr), & \text{for even } \ell,\\ 0, & \text{for odd } \ell.\end{cases} \tag{12}$$

The properties of $j_\ell(2qr)$, as a function of qr, are as follows. At low qr, the function starts out in the power form, $j_\ell(2qr) \approx (2qr)^\ell/\ell!!$, which is followed for $\ell \geqslant 2$ by a maximum at $qr \sim \frac{\ell}{2} + \frac{1}{4}$ and by a subsequent alternation at the approximate period of π. This has the following consequences for the ability to discern the source angular components S_ℓ. If R is a scale characterizing S_ℓ, then S_ℓ will have little impact on $\mathcal{R}_\ell$ if, at $\ell \geqslant 2$, qR falls into the hole in j_ℓ at low argument values. Likewise, S_ℓ will have little impact on $\mathcal{R}_\ell$ if many oscillations of j_ℓ are averaged over in the spatial integration over the source. The maximal impact is expected if qR falls into the region of the first maximum in j_ℓ; thus, most information on S_ℓ may be expected in $\mathcal{R}_\ell$ at $q \sim (\ell + \frac{1}{2})/(2R)$. Otherwise, the coefficients $\mathcal{R}_\ell$ are expected to behave as q^ℓ for low q and vanish at large q.

As characteristic for Fourier transforms, q and r enter the kernels as a product, and the low-r region of the source gets predominantly mapped onto the high-q region of the correlation function. Conversely, the high-r region of the source function mainly affects the low-q region of the correlation function. The inverse to the cosine Fourier transform is again the cosine Fourier transform, and the inverse to the spherical Bessel transform is the spherical Bessel transform. Given the Bessel function completeness relation

$$\int_0^\infty dq q^2 j_\ell(2qr) j_\ell(2qr') = \frac{\pi}{16}\delta(r - r'), \tag{13}$$

we can introduce an inverse kernel

$$\mathcal{K}_\ell^{-1}(r, q) = \begin{cases} \frac{(-1)^{\ell/2}}{\pi^3} j_\ell(2qr), & \text{for even } \ell, \\ 0, & \text{for odd } \ell, \end{cases} \tag{14}$$

and obtain

$$\mathcal{S}_{\vec{\ell}}(r) = 4\pi \int dq q^2 \mathcal{K}_\ell^{-1}(r, q)\mathcal{R}_{\vec{\ell}}(q). \tag{15}$$

B. Kernels for repulsive Coulomb interaction

The Coulomb final-state interaction also provides means for determining $\mathcal{S}(\boldsymbol{r})$ from $\mathcal{R}(\boldsymbol{q})$ [29,30]. In the Coulomb case, there is no straightforward way to invert the relation to the source function as in the case of pure interference. To understand how $\mathcal{S}$ impacts $\mathcal{R}$ for the Coulomb interaction, the structure of the kernel must be considered in detail.

In the classical limit of a repulsive Coulomb interaction, the kernel depends solely on θ_{qr} and on the ratio of the pair relative energy to the pair Coulomb energy at emission, namely,

$$x = \frac{Z_1 Z_2 e^2}{r}\frac{2\mu}{q^2} = \frac{r_C}{r}, \tag{16}$$

where μ is the reduced mass and r_C is the radius of the Coulomb barrier in the pair interaction. Quantal effects become important for $qr/\hbar$ of the order of unity. In the quantal situation, the kernel also depends on the dimensionless variable $qr/\hbar$. The Gamow factor parameter is then given by the parameter product $\eta = xqr/2 = Z_1 Z_2 e^2/v$ and a further parameter multiplication yields $x(qr)^2 = 2r/a_0$, where $a_0 = 1/Z_1 Z_2 e^2 \mu$ is the Bohr radius.

In the classical limit, the squared wave function represents the ratio of initial and final spatial densities during motion to the detectors for particles of a given initial momentum or, due to the conservation of phase-space density, the inverse ratio of the momentum densities at a fixed initial separation, that is,

$$\begin{aligned} |\phi^{(-)}(q, r, \cos\theta_{qr})|^2 \to \frac{d^3 r_\infty}{d^3 r} &= \frac{d^3 q_0}{d^3 q} \\ &= \frac{1 + \cos\theta_{qr} - x}{\sqrt{(1 + \cos\theta_{qr} - x)^2 - x^2}} \\ &\quad \times \Theta(1 + \cos\theta_{qr} - 2x). \end{aligned} \tag{17}$$

Here, $\boldsymbol{q}_0$ represents the relative momentum of the particles at separation $\boldsymbol{r}$, while $\boldsymbol{r}_\infty$ represents a remote separation of the particles at some instant when the relative momentum has approached $\boldsymbol{q}$. The right-hand-side result in Eq. (17) follows from Coulomb-trajectory considerations [29]. The implications of this result simplify [25] for $\ell = 0$ and in the high-energy ($x \ll 1$) and low-energy ($x \gg 1$) limits. Thus, for $\ell = 0$, the partial kernel is

$$\mathcal{K}_0(q, r) = \frac{q_0^2}{q^2}\frac{dq_0}{dq} - 1 = \frac{q_0}{q} - 1 = \frac{\Theta(x)}{\sqrt{1 - x}} - 1. \tag{18}$$

The three-dimensional kernel $\mathcal{K}$ is illustrated in Fig. 1 as a function of $\cos\theta_{qr}$, for two x values. In the high-energy limit of $x \ll 1$, the wave function squared $|\phi|^2$ is close to unity for most values of $\cos\theta_{qr}$. In that limit, the trajectories emerging from $\boldsymbol{r}$ are practically straight lines. The exception are the trajectories aiming toward the center of interaction that cannot penetrate the region of radius r_C. The trajectory directions with $\cos\theta_{qr} < -1 + 2x$ get shadowed. (The factor of 2 in front of x stems from the fact that trajectories get deflected both during the motion toward and away from the barrier.) The deflected trajectories pile up primarily outside of the shadowed region. The pileup produces an integrable singularity in the kernel as shown by the peaks in Fig. 1. At low ℓ, the Legendre polynomials have a limited angular resolution. Given that limited resolution, for the purpose of

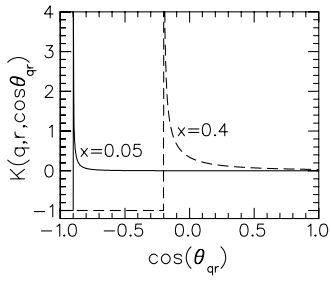

FIG. 1. Kernel $\mathcal{K}(q, r, \cos\theta_{qr}) = |\phi^{(-)}|^2 - 1$ for classical repulsive Coulomb interaction as a function of $\cos\theta_{qr}$ at two values of dimensionless parameter $x = r_C/r$, where $r_C = 2\mu Z_1 Z_2 e^2/q^2$. The structure around $\cos\theta_{qr} = -1$ is due to the deflection of classical trajectories directed toward the center of the repulsive Coulomb interaction. As the relative momentum within the pair increases, at fixed r, the range of backward angles where the kernel is significant shrinks.

the angular integration in Eq. (6), the angular structure in $|\phi|^2$ in the vicinity of the backward direction $\cos\theta_{qr} = -1$ may be approximated by a δ function multiplied by the integral over the structure, that is,

$$|\phi^{(-)}(q, r, \cos\theta_{qr})|^2 \approx 1 - \frac{x}{2}\delta(1 + \cos\theta_{qr}),$$

for

$$x \cdot \max(1, \ell) \ll 1. \tag{19}$$

Since $P_\ell(-1) = (-1)^\ell$, the high-energy kernel can be then approximated as

$$\mathcal{K}_\ell(q, r) \approx (-1)^{\ell+1} x/2,$$

for

$$x \ll 1/\max(1, \ell) \quad \text{and} \quad qr \gg \max(1, \ell). \tag{20}$$

For more implications of the classical limit (17) for kernels $\mathcal{K}_\ell$, see Ref. [25]. The classical limit of the Coulomb interaction is of interest in the context of emission of intermediate-mass fragments (IMF) from low-energy central nuclear reactions [30]. The practical condition of applicability for the classical approach is that $QR \gg \max(1, \ell)$, where Q is the characteristic momentum which yields $r_C \sim R$. With $Z \sim A/2$, this produces, at low ℓ, the condition $(e^2 A^3 m_N R)^{3/2} \gg 2$. Given a typical value of $R \sim 5$ fm for heavy ion reactions, this amounts to $A^{3/2} \gg 5$, and the classical limit is met at the fragment mass of $A \gtrsim 6$. IMF correlations are commonly expressed in terms of reduced velocity $v_{\rm red} = q/\mu(Z_1 + Z_2)^{1/2}$. With $Z \sim A/2$, $r_C \sim 2e^2/m_N v_{\rm red}$, and $R \sim 5$ fm, the high-energy limit of $x \ll 1$ for the kernel is reached at $v_{\rm red} \gtrsim 0.04\,c$.

At small qr in an interacting system, quantum effects become important as phase-space delocalization produces diffraction and tunneling. The diffraction affects the angle of an emerging particle at the level of $1/qr$, smearing out the angular structure in the kernel. Given the resolution of Legendre polynomials changing with ℓ, the diffraction effects become consequently important for $qr \lesssim \max(\ell, 1)$, with the kernel $\mathcal{K}_\ell$ then being reduced on average. The tunneling into the region of $x > 1$ becomes significant down to $r = 0$, for $2\eta = xqr \equiv qr_C \lesssim 1$. For singly charged particles, such as identical pions, this corresponds to $v \gtrsim 0.02c$. Unlike the classical expression (17), the Coulomb wave function squared

$$|\phi^{(-)}(q, r, \cos\theta_{qr})|^2 = G(\eta)|M(i\eta, 1, -iqr(1 + \cos\theta_{qr})|^2 \tag{21}$$

is analytic around $r = 0$ in the argument $r(1 + \cos\theta_{qr}) \equiv r + \boldsymbol{r} \cdot \hat{\boldsymbol{q}}$. In the quantal expression,

$$G(\eta) = \frac{2\pi\eta}{e^{2\pi\eta} - 1} \tag{22}$$

is the Gamow factor. The terms in the Taylor series for the squared wave function (21) behave as $r^\ell(1 + \cos\theta_{qr})^\ell$. Since the highest power of $\cos\theta_{qr}$ for an ℓth term is ℓ, the quantal Coulomb kernel $\mathcal{K}_\ell$ from Eq. (6) behaves around $r = 0$ as r^ℓ, similar to the identity-interference kernel (12). The power behavior associated with the quantal delocalization holds up to $r \lesssim \min(a_0, q^{-1})$. The behavior extends past the classical Coulomb barrier when $r_C \lesssim \min(a_0, q^{-1})$, leading to a further dampening of $\mathcal{K}_\ell$ at $\ell \geqslant 1$ in the barrier region.

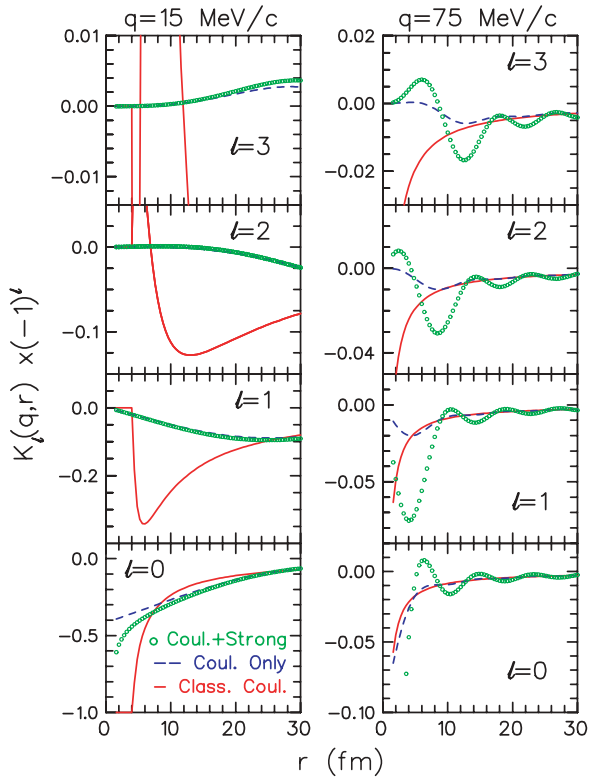

FIG. 2. (Color online) Kernels $\mathcal{K}_\ell$, multiplied by $(-1)^\ell$, for pK^+ interactions at $q = 15$ MeV/c (left panels) and $q = 75$ MeV/c (right panels), shown as a function of $1.5 < r < 30$ fm, for $\ell \leqslant 3$. Classical and quantal Coulomb kernels and quantal kernels with inclusion of strong interactions are represented by solid lines, dashed lines, and symbols, respectively. Vertical scale may change from panel to panel to emphasize details. Kernels are suppressed at the lowest r for the sake of clarity.

As an example, in Fig. 2, we consider $\mathcal{K}_\ell$ kernels for the pK^+ interaction. The kernels are shown for $\ell = (0\text{–}3)$, at relative momenta of $q = 15$ (left panels) and 75 MeV/c (right panels), as a function of distance r. Regions of higher and lower relative momenta within a correlation function $\mathcal{R}(q)$ are typically used to determine, respectively, about the short and long-range features of the source $\mathcal{S}(r)$. The solid lines, dashed lines, and symbols represent the classical Coulomb kernels, quantal Coulomb kernels, and quantal kernels with inclusion of strong interactions.

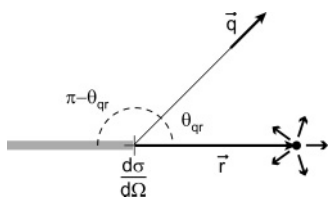

FIG. 3. In the asymptotic region of $r \to \infty$, for short-range interactions, the kernel K represents changes to the flux of particles emerging at relative momentum $\boldsymbol{q}$, produced by scattering. Here, the particles were initially separated by $\boldsymbol{r}$.

We first address the Coulomb kernels at 75 MeV/c. At large r in the right panels of Fig. 2, the classical Coulomb kernels $\mathcal{K}_\ell$ are, up to a sign, independent of ℓ and fall off as $1/r$, which is consistent with Eq. (20). Differences emerge at low r. At $\ell \geqslant 1$, the different classical kernels $\mathcal{K}_\ell$ switch sign $(\ell - 1)$ a number of times, cf. Ref. [25]. With the distance scale of r_C being, though, a fraction of a Fermi, $r_C = 0.17$ fm at $q = 75$ MeV/c, the structures associated with the sign switching are all pushed to very small r. Those sign-switching structures cannot be seen in the figure because the kernels at $r < 1.5$ fm are suppressed for the sake of clarity. For the quantum kernels, given $q^{-1} = 2.6$ fm, those kernels are seen to fluctuate with r around the classical kernels at $r \gg \max(1, \ell)q^{-1}$. At lower r and $\ell \geqslant 1$, quantal effects dampen the kernels; in particular, at very low r, the classical sign-switching in the kernels gets completely erased with the kernels behaving as r^ℓ. With inclusion of the effects of strong interactions in the kernels, additional oscillations are observed with r within the figure, as the asymptotic behavior of the partial-wave functions changes for low angular momenta, producing wave-function distortions at moderate distances. We will focus on strong interactions in the next subsection.

At $q = 15$ MeV/c, the classical Coulomb radius rises to $r_C = 4.1$ fm, on one hand, pushing the asymptotic high-energy region out of the r range shown in Fig. 2 and, on the other hand, making some of the low-r details of the classical Coulomb kernels visible within the shown range. Also, since $q^{-1} = 13.1$ fm, much of the region for the left panels of Fig. 2 is dominated by quantal effects. The kernels with inclusion of strong interactions get to be very close to the Coulomb kernels, since the phase shifts characterizing changes in the partial-wave asymptotic behavior are close to zero at low q.

The quantal suppression of the kernels at $qr \lesssim \ell$, progressing with ℓ, makes it difficult to learn about the directional characteristics of a source from the particle correlations at low $q \lesssim R^{-1} = 40$ MeV/c for $R = 5$ fm. Small kernels produce small contributions to the correlation which are difficult to detect experimentally. At the other end, at high qr, while the kernels become independent of ℓ, they also become small, falling off as $1/(q^2 r)$, cf. Eq. (20). As a consequence, an optimal bracket of q emerges for accessing the directional characteristic of sources with typical size, such as $q \sim (30 - 100)$ MeV/c for the pK^+ system.

We have seen the importance of the analyticity of $|\phi|^2$ in r around $r = 0$, which implied the r^ℓ suppression of the $\mathcal{K}_\ell (\ell \geqslant 1)$ kernels at low r. The analyticity in q is of interest in the context of the analysis of correlation functions as a function of $\boldsymbol{q}$. In the case of pure identity interference, the wave function squared (11) is analytic in $\boldsymbol{q}$, which makes the kernels from Eq. (3) analytic in $\boldsymbol{q}$. The resulting correlation coefficients $\mathcal{R}_\ell$ are also analytic and behave as q^ℓ at small q. In contrast, because of the general dependence on the parameter

$$\eta = \frac{Z_1 Z_2 e^2 \mu}{q}, \tag{23}$$

inversely proportional to q, and because of the appearance of the Gamow factor (22), the square of the Coulomb wave function (21) lacks analyticity in $\boldsymbol{q}$ around $q = 0$. Still, it may be tempting to factor out the Gamow factor, as has been done in the analysis of pion correlations, arriving, with $|\phi|^2/G \equiv |M|^2$, at a Gamow-corrected kernel. The corrected kernel remains finite at a given r and θ_{rq}, when $q \to 0$, but retains a dependence in this limit on $\cos\theta_{qr}$ for any finite value of r. Thus, $|M|$ reaches a different value depending on the side from which $q = 0$ is reached and lacks therefore analyticity in $\boldsymbol{q}$. Correspondingly, even the Gamow-corrected correlation functions from Eq. (3) lack analyticity in $\boldsymbol{q}$. The Gamow-corrected kernels $\mathcal{K}_\ell$ tend to finite values as $q \to 0$, rather than behaving as q^ℓ.

As to the high-q limit of the Coulomb kernels, while the resolving power becomes independent of ℓ, the accessed information on the source represents one moment only per correlation coefficient, as

$$\mathcal{R}_{\ell m}(q) \underset{q\to\infty}{\approx} \frac{2\sqrt{\pi}(-1)^\ell Z_1 Z_2 e^2 \mu}{q^2} \left\langle \frac{1}{r} Y^*_{\ell m}(\Omega) \right\rangle, \tag{24}$$

$$\mathcal{R}_{\bar{\ell}}(q) \underset{q\to\infty}{\approx} \frac{(-1)^\ell Z_1 Z_2 e^2 \mu}{q^2} \left\langle \frac{1}{r} \mathcal{A}_{\bar{\ell}}(\Omega) \right\rangle, \tag{25}$$

where

$$\langle F \rangle = \int d^3 r \mathcal{S}(\boldsymbol{r}) F(\boldsymbol{r}). \tag{26}$$

Since the classical approximation is accurate at large qr, this relation is unchanged by quantum considerations. Working within the classical approximation, one might be tempted to continue the r_C/r kernel expansion, producing expansion of the correlation in powers of $1/q^2$. The next expansion term could give access to the moment of the source function with a factor of $1/r^2$ in place of $1/r$. However, beyond the leading term, the expansion gets altered by quantum effects, making the expectation invalid for lighter particle pairs such as pK^+.

C. Kernels for short-range interactions

Strong interactions between two particles also provide leverage for extracting source information from measured correlations and are particularly effective when the strong-interaction cross sections are large [29]. In analyzing the effects of the interaction, the two-particle scattering wave function may be conveniently decomposed into angular-momentum eigenstates, here with any intrinsic spins suppressed

$$\begin{aligned} \phi^{(-)}(q, r, \cos\theta_{qr}) &= \sum_{\ell_1} a_{\ell_1} \frac{R_{\ell_1}(r)}{r} P_{\ell_1}(\cos\theta_{qr}) \\ &\underset{r\to\infty}{\approx} \exp(iqr\cos\theta_{qr}) + f^*(\pi - \theta_{qr}) \\ &\quad \times \frac{\exp(-iqr)}{r}. \end{aligned} \tag{27}$$

The coefficients a_ℓ in front of the radial wave functions R_ℓ are adjusted to make the large-r *outgoing* wave contributions to $\phi^{(-)}$ identical to those for a wave in the absence of short-range interactions. The explicit asymptotic form of the wave function, on the right-hand side, is shown for the case with no Coulomb interactions. The amplitude $f \equiv f^{(+)}$ is the scattering amplitude associated with the more standard scattering wave function $\phi^{(+)}$ where conditions are imposed onto *incoming* wave contributions in the asymptotic region.

The amplitude factors in the two wave functions are related with $f^{(-)}(\theta) = [f^{(+)}(\pi - \theta)]^*$.

The three-dimensional kernel from Eq. (27) is

$$\mathcal{K}(q, r, \cos\theta_{qr}) \equiv |\phi^{(-)}|^2 - 1 = \frac{1}{r^2}\sum_{\ell_1\ell_2} a_{\ell_1} a^*_{\ell_2} R_{\ell_1}(r) R_{\ell_2}(r) \times P_{\ell_1}(\cos\theta_{qr}) P_{\ell_2}(\cos\theta_{qr}) - 1. \tag{28}$$

Since most shape information is contained at intermediate to large r, the large-r limit is especially insightful and can be found from Eq. (27) to be

$$\mathcal{K}(q, r, \cos\theta_{qr}) \underset{r\to\infty}{\approx} \frac{1}{r^2}\frac{d\sigma}{d\Omega}(\pi - \theta_{qr}) - \frac{\mathrm{Im}\, f(\pi - \theta_{qr})}{r}\sin[qr(1 + \cos\theta_{qr})] + \frac{\mathrm{Re}\, f(\pi - \theta_{qr})}{r}\cos[qr(1 + \cos\theta_{qr})] \tag{29}$$

$$\to \frac{1}{r^2}\frac{d\sigma}{d\Omega}(\pi - \theta_{qr}) - \frac{\sigma}{2\pi r^2}\delta(1 + \cos\theta_{qr}). \tag{30}$$

In arriving at Eqs. (29) and (30), we used an expression for the scattering cross section, $|f|^2 = d\sigma/d\Omega$, and the optical theorem, $\mathrm{Im} f(0) = q\sigma/4\pi$. Furthermore, in obtaining the expression (30) we exploited the fact that for $qr \to \infty$, under an $\boldsymbol{r}$ integration, the respective products in Eq. (29) approach the limits $qr\sin(qrx) \to \delta(x)$ and $qr\cos(qrx) \to 0$. As illustrated in Fig. 3, the result [Eq. (30)] has a simple geometric interpretation. The first term represents the probability that a particle aimed directly at the scatterer reflects into the direction of $\boldsymbol{q}$, while the negative term represents the shadowing of a spherical angle, $\sigma/4\pi r^2$, around the backward direction.

The partial kernels $\mathcal{K}_\ell$, respectively, from Eqs. (28) and (30), are

$$\mathcal{K}_\ell(q, r) = \frac{1}{r^2}\sum_{\ell_1\ell_2}\begin{pmatrix} \ell & \ell_1 & \ell_2 \\ 0 & 0 & 0 \end{pmatrix}^2 a_{\ell_1} a^*_{\ell_2} R_{\ell_1}(r) R_{\ell_2}(r) - \delta_{\ell 0} \tag{31}$$

$$\underset{r\to\infty}{\approx} \frac{(-1)^\ell}{r^2}\left[\frac{1}{2}\int d\cos\theta\, P_\ell(\cos\theta)\frac{d\sigma}{d\Omega}(\theta) - \frac{\sigma}{4\pi}\right], \tag{32}$$

where we have made use of the Wigner $3j$ symbol. In the asymptotic region, all $\ell \geqslant 1$ kernels decrease as $1/r^2$ and are proportional to the scattering cross section. Larger cross sections, such as those associated with resonances, will lead to larger kernels at a given q. Otherwise, the kernels are sensitive to the angular dependence of the cross sections. For q in the range for which correlations are typically studied, cross sections are usually fairly isotropic. Thus, the first term in the brackets on the right-hand side of Eq. (32) decreases quickly as ℓ increases, yielding

$$\mathcal{K}_\ell(q, r) \approx \frac{(-1)^{\ell+1}\sigma}{4\pi r^2} \tag{33}$$

for large r and ℓ. Apart from the sign, this kernel is independent of ℓ, similar to the Coulomb kernel in Eq. (20). In analogy to the classical Coulomb results for individual ℓ, the asymptotic results [Eq. (32)] require $qr \gg \ell$ for their validity. An additional condition for validity is that $r/d \gg \ell$, where d is the interaction range.

Regarding the limiting short-range [Eq. (33)] and Coulomb [Eq. (20)] $\mathcal{K}_\ell$ results, their independence from ℓ results from the kernels being exclusively influenced by the shadowing of particles by each other. The effect of shadowing decreases with distance between the particles, but more slowly for the Coulomb than for the purely short-range interaction. For short-range interactions, the kernel falls off as σ/r^2; while for Coulomb forces., the kernels fall off as r_C/r, where $r_C = 2\mu Z_1 Z_2 e^2/q^2$ is the radius of the Coulomb barrier. Since r_C explicitly decreases with q, Coulomb kernels decrease monotonically with increasing q; whereas for the strong interaction, the q dependence on the kernel tends to follow the energy dependence of the cross section. Strong interactions can thus provide resolving power at large q, if the cross sections are large, e.g., at resonance energies.

When the two terms in the asymptotic form of the kernel in Eq. (30) are integrated over the full spherical angle, those terms exactly cancel, reflecting the fact that for a short-range interaction, the particles which are shadowed for $\cos\theta_{qr} = -1$ reappear at other angles at the same magnitude of relative momentum. Consequently, the $\ell = 0$ coefficient for the $1/r^2$ asymptotic falloff in Eq. (32) vanishes, implying that the $\mathcal{K}_0$ kernel from Eq. (31) vanishes faster than $1/r^2$ as $r \to \infty$. These results may be contrasted with what is found for the Coulomb interactions. The large-r Coulomb kernel from Eq. (19) yields a finite result when integrated over the spherical angle. In direct consequence, the $\ell = 0$ kernel is finite in the asymptotic region [Eqs. (18) and (20)]. The difference between the short-range and Coulomb cases is due to the fact that a Coulomb interaction does not just change the orientation of the relative momentum but also makes the momentum magnitude different from the asymptotic value at any finite distance from the interaction center.

At low relative momenta q, s-wave scattering is likely to dominate. An important result, visible already in the asymptotic limit [Eqs. (32) and (33)], is that the s-wave scattering contributes to the kernels at all ℓ. At the level of Eq. (31), it is associated with the interference between the waves. At resonance, the radial wave functions R_ℓ will be particularly large in the near zone giving rise to enhanced $\mathcal{K}_\ell$ there, including $\ell = 0$. At low q and finite ℓ, the effects of the centrifugal barrier can be important. When q is so low that the barrier is encountered outside of the strong-interaction range, $qr < \ell + \frac{1}{2}$ at $r > d$, the radial wave functions are approximately given in terms of the spherical Bessel functions, $R_\ell/r \propto j_\ell(qr) \propto (qr)^\ell$. With R_0 approaching a constant value as a function of both q and r in the region $d < r \ll 1/q$, at $q \to 0$, given the triangle inequality for the ℓ values in the $3j$ symbol in Eq. (32), the strong-interaction kernels will behave as $\mathcal{K}_\ell(q, r) \propto (qr)^\ell(1 + b/r)$ for $\ell \geqslant 1$ in the region. The kernels will be suppressed then at low q and low r as well as for larger ℓ. A short-range repulsion may enhance suppression at the lowest $r < d$ beyond that produced by the centrifugal barrier.

Outside of the interaction range, at $r > d$, the wave functions R_ℓ are fully determined by the respective strong-interaction phase shifts, both in the absence and presence

of Coulomb interactions. We exploit this [29] in obtaining the kernels for strong interactions, e.g., the kernels in Fig. 2. Energy derivatives additionally constrain the integrals of the wave functions R_ℓ squared over the region $r < d$ [29,31]. This facilitates an extrapolation of the kernels down to $r = 0$, adequate for source resolutions that can be practically achieved, without the need to resort to potential models for the strong interaction. Still, with the strong-interaction kernels becoming model dependent at short distances, we refrain from displaying them at $r < 1.5$ fm. Needless to say, that given the quark substructure of hadrons, the description in terms of wave function for relative motion becomes questionable at the shortest distances $r \lesssim 0.5$ fm. For IMFs the same becomes true at even larger distances, because of the finite size of the nuclei.

III. SPHERICAL CARTESIAN HARMONICS

A. Harmonics within spherical coordinates

We start out with a review of basic concepts concerning surface spherical harmonics. A harmonic function is one that satisfies the Laplace equation

$$\nabla^2 F(\boldsymbol{r}) = 0. \tag{34}$$

When using spherical coordinates, it is convenient to express harmonic functions, which are regular at the origin, in terms of tesseral harmonics $Y_{\ell m}$,

$$F(\boldsymbol{r}) = \sqrt{4\pi} \sum_{\ell m} F^*_{\ell m} r^\ell Y_{\ell m}(\Omega), \tag{35}$$

where the coefficients $F_{\ell m}$ take on arbitrary values. In the summation over ℓ, the individual terms in Eq. (35), of the form

$$F^{(\ell)}(\boldsymbol{r}) = \sqrt{4\pi} r^\ell \sum_{m} F^*_{\ell m} Y_{\ell m}(\Omega), \tag{36}$$

are harmonic functions of degree ℓ. The latter stand for homogenous functions of degree ℓ in x, y, and z that are harmonic. A surface spherical of degree ℓ is a harmonic function of degree ℓ, taken on a unit sphere, $r = 1$:

$$F^{(\ell)}(\Omega) = \sqrt{4\pi} \sum_{m} F^*_{\ell m} Y_{\ell m}(\Omega). \tag{37}$$

Given the completeness relation for the tesseral spherical harmonics,

$$\begin{aligned}\delta(\Omega - \Omega') &= \frac{1}{4\pi} \sum_{\ell} (2\ell + 1) P_\ell(\boldsymbol{n} \cdot \boldsymbol{n}') \\ &= \sum_{\ell m} Y^*_{\ell m}(\Omega') Y_{\ell m}(\Omega),\end{aligned} \tag{38}$$

any function of spherical angle, and in particular $\mathcal{R}$ and $\mathcal{S}$ in Eqs. (8)–(10), can be expanded in the tesseral harmonics upon using Eq. (38) with the identity

$$G(\Omega) = \int d\Omega' \delta(\Omega - \Omega') G(\Omega'). \tag{39}$$

Equation (35) for the harmonic functions represents an example of the expansion in which the expansion coefficients have a specific radial dependence. Within every rank ℓ of an expansion, the expanded functions are generally described in terms of $(2\ell + 1)$ complex coefficients $F_{\ell m}$. However, for real expanded functions, the coefficients $F_{\ell, m=0}$ must be real; otherwise, the coefficients must satisfy $F_{\ell -m} = (-1)^m F^*_{\ell m}$. Thus, for each ℓ, the expansion is described in terms $(2\ell + 1)$ independent real numbers. Under rotations of the coordinate system for a given ℓ, the tesseral functions transform like the components of a spherical tensor of rank ℓ. For a function that is independent of the coordinate choice, the expansion coefficients transform further in this fashion; the sums over m in Eqs. (35), (36), and (5) represent scalar products of the spherical tensors. In fact, the right-hand side of Eq. (38) also represents a superposition of the scalar products and, in this, represents a covariant generalization of the middle result in Eq. (38), which is seen as a superposition of the scalar products of the tensors in the case when the coordinate z axis is oriented either along $\boldsymbol{n}$ or $\boldsymbol{n}'$.

B. Cartesian harmonics

Cartesian harmonics allow functions of the spherical angle to be expressed as superpositions of the scalar products of Cartesian tensors. For real functions, the coefficients of expansion in Cartesian harmonics are real, which is not necessarily the case when expanding functions in tesseral harmonics. The expansion coefficients for Cartesian harmonics are generally easier to interpret than those for tesseral harmonics.

Let us consider a homogenous function of degree ℓ. When using Cartesian coordinates, a homogenous function may be represented as

$$F^{(\ell)}(\boldsymbol{r}) = \sum_{\alpha_1 \alpha_2 \ldots \alpha_\ell} F^{(\ell)}_{\alpha_1 \alpha_2 \ldots \alpha_\ell} r_{\alpha_1} r_{\alpha_2} \ldots r_{\alpha_\ell}, \tag{40}$$

where $\alpha = x, y, z$ are Cartesian indices. The following remarks can be made regarding this representation in terms of Cartesian coordinates. Since the product of Cartesian coordinates on the right-hand side of Eq. (40) is symmetric under the interchange of its terms, attention may be limited to the coefficients of expansion $F_{\alpha_1 \alpha_2 \ldots \alpha_\ell}$ which are symmetric under the interchange of indices. Since the product of ℓ coordinates transforms further as a Cartesian tensor of rank ℓ, the coefficients $F_{\alpha_1 \alpha_2 \ldots \alpha_\ell}$ must transform as a Cartesian tensor of rank ℓ for a function $F^{(\ell)}$ that is independent of the choice of directions for coordinate axes. Given the symmetry of the tensorial coefficients, the right-hand side of Eq. (40) can be conveniently rewritten by grouping terms with different numbers, ℓ_x, ℓ_y, and ℓ_z, respectively, of the x, y, and z coefficients, obtaining the representation such as in Eq. (8),

$$F^{(\ell)}(\boldsymbol{r}) = \sum_{\vec{\ell}} \frac{\ell!}{\ell_x! \ell_y! \ell_z!} F_{\vec{\ell}} x^{\ell_x} y^{\ell_y} z^{\ell_z} \equiv F^\top \boldsymbol{r}^\ell, \tag{41}$$

where $\ell = \ell_x + \ell_y + \ell_z$. The last expression in Eq. (41) is a schematic representation for the convolution of the Cartesian tensors.

On substituting the representation (40) into the Laplace equation (34), we find that the homogenous function is harmonic if and only if the Cartesian tensorial coefficients

are traceless [12], i.e.,

$$\sum_{\alpha} F^{(\ell)}_{\alpha_1 \ldots \alpha_{\ell-2}\alpha\alpha} = 0, \tag{42}$$

or

$$F_{\ell_x+2,\ell_y,\ell_z} + F_{\ell_x,\ell_y+2,\ell_z} + F_{\ell_x,\ell_y,\ell_z+2} = 0, \tag{43}$$

where $\ell_x + \ell_y + \ell_z + 2 = \ell$. The components for a symmetric tensor, labeled with the values of (ℓ_x, ℓ_y, ℓ_z), are illustrated with a triangle in Fig. 4. When moving along lines parallel to the different sides of the triangle, either the value of ℓ_x, ℓ_y, or ℓ_z stays constant. The tracelessness condition (43) relates components at the corners of an equilateral triangle two ℓ units on the side in the figure.

In the Appendix, we show that there exists a real projection operator $\mathcal{P}$, which operates in the space of Cartesian tensors of rank ℓ and projects, out of any tensor, the part which is symmetric and traceless. As an operator in the space of rank ℓ tensors, $\mathcal{P}$ itself is a rank 2ℓ tensor, ℓ times covariant and ℓ times contravariant. As a projection operator, $\mathcal{P}$ satisfies $\mathcal{P}^2 = \mathcal{P}$ and $\mathcal{P}^\top = \mathcal{P}$. In terms of the operator $\mathcal{P}$, for any tensor T of rank ℓ, the function given by

$$(\mathcal{P}T)^\top \boldsymbol{r}^\ell = T^\top \mathcal{P}^\top \boldsymbol{r}^\ell = T^\top \mathcal{P}\boldsymbol{r}^\ell \tag{44}$$

is harmonic, where we follow the schematic notation. Since the function (44) is harmonic for any tensor T, each of the components of $\mathcal{P}\boldsymbol{r}^\ell$ on the right-hand side must be harmonic.

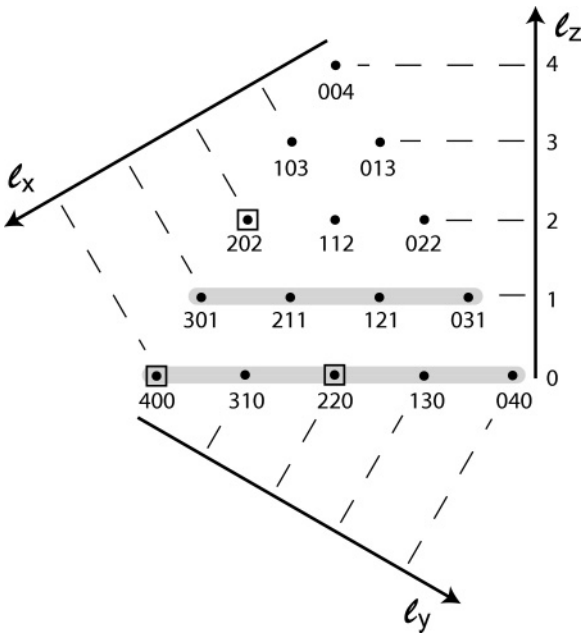

FIG. 4. Triangular diagram representing the components of a symmetric tensor, in terms of dots labeled with the component $[\ell_x, \ell_y, \ell_z]$ values, for $\ell = \ell_x + \ell_y + \ell_z = 4$, after Ref. [26]. When moving along the lines parallel to the respective sides of the triangle, either ℓ_x, ℓ_y, or ℓ_z stays constant. The tracelessness condition (43) relates tensor components at the corners of an equilateral triangle two ℓ units on the side, within the diagram, such as those marked by the squares. As the set of linearly independent components of a traceless symmetric tensor, the $\ell_z = 0$ and $\ell_z = 1$ components may be chosen (thick grey lines).

On the sphere of $r = 1$, those components define the Cartesian surface spherical harmonics

$$\mathcal{A}^{(\ell)}_{\alpha_1\alpha_2\ldots\alpha_\ell}(\Omega) = \sum_{\alpha'_1\alpha'_2\ldots\alpha'_\ell} \mathcal{P}^{(\ell:\ell)}_{\alpha_1\alpha_2\ldots\alpha_\ell:\alpha'_1\alpha'_2\ldots\alpha'_\ell} n_{\alpha'_1} n_{\alpha'_2} \ldots n_{\alpha'_\ell}, \tag{45}$$

where $\boldsymbol{n} = (\sin\theta\cos\phi, \sin\theta\sin\phi, \cos\theta)$, which can be further also written as

$$\mathcal{A}_{\vec{\ell}}(\Omega) = \sum_{\vec{\ell}'} \frac{\ell!}{\ell'_x!\ell'_y!\ell'_z!} \mathcal{P}_{\vec{\ell}:\vec{\ell}'} n_x^{\ell'_x} n_y^{\ell'_y} n_z^{\ell'_z}. \tag{46}$$

Cartesian components of the direction vector $\boldsymbol{n}$ are combinations of the tesseral rank-1 harmonics Y_{1m}. The product of ℓ components as, e.g., demonstrated by the quantal rules of angular-momentum superposition is a superposition of tesseral harmonics of rank ℓ and lower, of the same evenness as ℓ:

$$n_{\alpha_1} n_{\alpha_2} \ldots n_{\alpha_\ell} = \sum_{\ell' m' \ell' \leqslant \ell} c^{\ell' m' *}_{\alpha_1\alpha_2\ldots\alpha_\ell} Y_{\ell' m'}(\Omega) \equiv \mathcal{A}^{(\ell)}_{\alpha_1\alpha_2\ldots\alpha_\ell} + \left(n_{\alpha_1} n_{\alpha_2} \ldots n_{\alpha_\ell} - \mathcal{A}^{(\ell)}_{\alpha_1\alpha_2\ldots\alpha_\ell}\right). \tag{47}$$

Since $r^\ell \mathcal{A}^{(\ell)}$ are harmonic, $\mathcal{A}^{(\ell)}$ can consist of the tesseral rank-ℓ harmonics only. As will be demonstrated in the Appendix, the operator $\mathcal{P}$ consists of a symmetrization operator, i.e., the unit tensor in the space of symmetric Cartesian tensors, and of operator terms that involve taking traces of one or more pairs of the Cartesian indices. In acting on the the Cartesian product $\boldsymbol{n}^\ell$, the symmetrization operator leaves the product $\boldsymbol{n}^\ell$ intact, while the other operator terms in $\mathcal{P}$ produce symmetrized terms of the form $\boldsymbol{n}^{\ell-2k}(\delta)^k$, where $k = 1, \ldots, \ell/2$. The latter terms represent superpositions of tesseral harmonics up to the rank of $\ell - 2$, of the same evenness as ℓ. The implication is that the projection operator $\mathcal{P}$ removes from $\boldsymbol{n}^\ell$ a portion represented by the superposition of the lower rank tesseral harmonics [in parenthesis on the right-hand side of Eq. (47)] while retaining the highest rank ℓ portion intact. Given the general form of $\mathcal{A}^{(\ell)}$, from application of $\mathcal{P}$ onto $\boldsymbol{n}^\ell$, the Cartesian harmonics may be constructed recursively [25], based on the tracelessness of the $\mathcal{A}^{(\ell)}$ tensors within each rank, starting with $\mathcal{A}^{(\ell=0)} = 1$:

$$\mathcal{A}^{(\ell)}_{\alpha_1\cdots\alpha_\ell} = \frac{1}{\ell}\sum_{i=1}^{\ell} n_{\alpha_i} \mathcal{A}^{(\ell-1)}_{\alpha_1\cdots\alpha_{i-1}\alpha_{i+1}\cdots\alpha_\ell} - \frac{2}{\ell(2\ell-1)} \times \sum_{1 \leqslant i < j \leqslant \ell} \sum_{\alpha} \delta_{\alpha_i\alpha_j} n_\alpha \mathcal{A}^{(\ell-1)}_{\alpha\alpha_1\cdots\alpha_{i-1}\alpha_{i+1}\cdots\alpha_{j-1}\alpha_{j+1}\cdots\alpha_\ell}. \tag{48}$$

Expressions for Cartesian harmonics of lowest rank are given in Table I, and the recursion with Eq. (48), otherwise, produces the series in Eq. (7). One of the features of the Cartesian harmonics is that the three Cartesian axes are treated equally, unlike in the case of tesseral harmonics. Within a given rank ℓ, not all Cartesian harmonics are independent. A symmetric tensor has $(\ell+1)(\ell+2)/2$ different components, cf. Fig. 4. The tracelessness condition (44) reduces the number of linearly independent components, including the number of independent $\mathcal{A}^{(\ell)}$ functions, to $(2\ell+1)$, equal to the number of $Y_{\ell m}$ functions. As a linearly independent set, one might choose the components with $\ell_z = 0$ and $\ell_z = 1$, see the figure.

TABLE I. Cartesian harmonics for $\ell \leqslant 4$. Other harmonics can be found by either permuting the indices, i.e., $\mathcal{A}_{xyx} = \mathcal{A}_{xxy}$, or by swapping indices on both sides of an equality, e.g., $x \leftrightarrow y$. Thus, given $\mathcal{A}_{xxy} = n_x^2 n_y - (1/5)n_y$, swapping the indices $y \leftrightarrow z$ yields $\mathcal{A}_{xxz} = n_x^2 n_z - (1/5)n_z$.

$\mathcal{A}^{(1)}_x = n_x$	$\mathcal{A}^{(3)}_{xyz} = n_x n_y n_z$
$\mathcal{A}^{(2)}_{xx} = n_x^2 - 1/3$	$A^{(4)}_{xxxx} = n_x^4 - (6/7)n_x^2 + 3/35$
$\mathcal{A}^{(2)}_{xy} = n_x n_y$	$\mathcal{A}^{(4)}_{xxxy} = n_x^3 n_y - (3/7)n_x n_y$
$A^{(3)}_{xxx} = n_x^3 - (3/5)n_x$	$\mathcal{A}^{(4)}_{xxyy} = n_x^2 n_y^2 - (1/7)n_x^2 - (1/7)n_y^2 + 1/35$
$\mathcal{A}^{(3)}_{xxy} = n_x^2 n_y - (1/5)n_y$	$\mathcal{A}^{(4)}_{xxyz} = n_x^2 n_y n_z - (1/7)n_y n_z$

In the case of $\alpha_1 = \alpha_2 = \ldots = \alpha_\ell = z$ in Eq. (47), both the Cartesian component product $\boldsymbol{n}^\ell$ and $\mathcal{A}^{(\ell)}$ are invariant with respect to rotations around the z axis. For invariance, both functions must be a superposition of $m' = 0$ tesseral harmonics only. It follows then that $\mathcal{A}^{(\ell)}_{z\ldots z}$ must be proportional to $Y_{\ell 0}$ or P_ℓ. Since the action of the projection operator $\mathcal{P}$ leaves the highest rank terms unchanged, the coefficient for P_ℓ in $\mathcal{A}^{(\ell)}$ must be the same as in $\boldsymbol{n}^\ell$. Accordingly, the respective Cartesian harmonics are given by

$$\mathcal{A}^{(\ell)}_{zz\ldots z}(\Omega) = \frac{\ell!}{(2\ell-1)!!} P_\ell(\cos\theta). \tag{49}$$

Starting with the first equality in Eq. (38), we are now in position to produce a completeness relation in terms of the Cartesian harmonics. Thus, if $\boldsymbol{n}'$ is directed along the z axis in Eq. (38), we can express, given Eq. (49), the Legendre polynomial in the middle term in Eq. (38) as $[(2\ell-1)!!/\ell!](\boldsymbol{n}'^\ell)^\top \mathcal{A}$. When rotating $\boldsymbol{n}'$ and $\boldsymbol{n}$, to move $\boldsymbol{n}'$ away from the alignment with the z axis, the scalar product of the tensors transforms covariantly, allowing us to obtain different general representations for the δ function in spherical angle in terms of the Cartesian harmonics:

$$\begin{aligned}
\delta(\Omega - \Omega') &= \frac{1}{4\pi}\sum_\ell (2\ell+1) P_\ell(\boldsymbol{n}\cdot\boldsymbol{n}') \\
&= \frac{1}{4\pi}\sum_\ell \frac{(2\ell+1)!!}{\ell!} \sum_{\alpha_1\ldots\alpha_\ell} n'_{\alpha_1}\ldots n'_{\alpha_\ell} \mathcal{A}^{(\ell)}_{\alpha_1\ldots\alpha_\ell}(\Omega) \\
&= \frac{1}{4\pi}\sum_\ell \frac{(2\ell+1)!!}{\ell!} \sum_{\alpha_1\ldots\alpha_\ell} \mathcal{A}^{(\ell)}_{\alpha_1\ldots\alpha_\ell}(\Omega') \mathcal{A}^{(\ell)}_{\alpha_1\ldots\alpha_\ell}(\Omega) \\
&= \frac{1}{4\pi}\sum_{\vec{\ell}} \frac{(2\ell+1)!!}{\ell_x!\ell_y!\ell_z!} \mathcal{A}_{\vec{\ell}}(\Omega') \mathcal{A}_{\vec{\ell}}(\Omega) \\
&= \frac{1}{4\pi}\sum_{\vec{\ell}} \frac{(2\ell+1)!!}{\ell_x!\ell_y!\ell_z!} \mathcal{A}_{\vec{\ell}}(\Omega') n_x^{\ell_x} n_y^{\ell_y} n_z^{\ell_z}.
\end{aligned} \tag{50}$$

In obtaining the third equality in Eq. (50) and later, we use the projection properties of the operator $\mathcal{P}$:

$$(\boldsymbol{n}'^\ell)^\top \mathcal{A} = (\boldsymbol{n}'^\ell)^\top \mathcal{P}\mathcal{A} = (\mathcal{P}\boldsymbol{n}'^\ell)^\top \mathcal{A} = (\mathcal{A}')^\top \mathcal{A}. \tag{51}$$

Use of Eq. (50) in the identity (39) allows functions of the spherical angle to be expressed as a sum of Cartesian harmonics, such as in Eq. (8). Independent of the orientation of the coordinate axes, the coefficients of expansion in Cartesian harmonics, such as in Eq. (9), transform as components of a Cartesian tensor under rotations. As the tensor is traceless, only $(2\ell+1)$ coefficients are independent within each rank ℓ.

C. Operations with Cartesian harmonics

When given some specific expansion coefficients in terms of Cartesian harmonics, it may be of interest to calculate the associated Cartesian moments. To facilitate that, it is useful to express products of Cartesian components in terms of Cartesian harmonics, which can be done [25] through recursion starting from Eq. (7), obtaining

$$\begin{aligned}
n_x^{\ell_x} n_y^{\ell_y} n_z^{\ell_z} = \sum_{\substack{\vec{m} \\ 0 \leqslant m_i \leqslant \ell_i/2}} & \frac{(2\ell-4m+1)!!}{2^m(2\ell-2m+1)!!} \frac{\ell_x!}{(\ell_x-2m_x)!m_x!} \\
& \times \frac{\ell_y!}{(\ell_y-2m_y)!m_y!} \frac{\ell_z!}{(\ell_z-2m_z)!m_z!} \mathcal{A}_{\vec{\ell}-2\vec{m}}(\Omega).
\end{aligned} \tag{52}$$

The rank of $\mathcal{A}$ within each Cartesian component on the right-hand side is equal to or lower than the power of the corresponding Cartesian component on the left-hand side. From Eqs. (52) and (9), we find

$$\begin{aligned}
&\int d^3r \mathcal{S}(\boldsymbol{r}) x^{\ell_x} y^{\ell_y} z^{\ell_z} \\
&\quad = \frac{4\pi\ell!}{(2\ell+1)!!} \sum_{\substack{\vec{m} \\ 0 \leqslant m_i \leqslant \ell_i/2}} \frac{(2\ell-4m+1)!!}{2^m(2\ell-2m+1)!!} \\
&\qquad \times \frac{\ell_x!}{(\ell_x-2m_x)!m_x!} \frac{\ell_y!}{(\ell_y-2m_y)!m_y!} \frac{\ell_z!}{(\ell_z-2m_z)!m_z!} \\
&\qquad \times \int_0^\infty dr r^{\ell+2} \mathcal{S}_{\vec{\ell}-2\vec{m}}(r),
\end{aligned} \tag{53}$$

which allows the moments to be obtained from Cartesian harmonic coefficients.

As combinations of tesseral harmonics of different rank ℓ, the Cartesian harmonics of different rank are orthogonal to one another. Due to different behavior under inversion, see Eq. (7), two Cartesian harmonics are further orthogonal if any pair of their ℓ_i subscripts differs by an odd number. Otherwise, the scalar product of harmonics is given by [26]

$$\begin{aligned}
\langle \vec{\ell} | \vec{\ell}' \rangle \equiv \int \frac{d\Omega}{4\pi} \mathcal{A}_{\vec{\ell}} \mathcal{A}_{\vec{\ell}'} &= \frac{1}{(2\ell+1)!!(2\ell-1)!!} \\
&\times \sum_{\substack{\vec{m} \\ \max(0,(\ell'_i-\ell_i)/2) \leqslant m_i \\ m_i \leqslant \min(\ell'_i-\ell_i/2, \ell_i/2)}} \left(-\frac{1}{2}\right)^m m!(2\ell-2m-1)!! \\
&\times \prod_{i=x,y,z} \frac{\ell_i!\ell'_i!}{((\ell'_i-\ell_i)/2+m_i)!(\ell_i-2m_i)!m_i!}.
\end{aligned} \tag{54}$$

The anticipated symmetry between $\vec{\ell}$ and $\vec{\ell}'$ on the right-hand side of Eq. (54) may be seen by eliminating m_i in favor of $m'_i = m_i + (\ell_i - \ell'_i)/2$.

Cartesian expansion coefficients may be converted into tesseral expansion coefficients and vice versa. In terms of

Cartesian harmonics, the $m \geqslant 0$ tesseral harmonics are given by [26]

$$Y_{\ell m}(\Omega) = (-1)^m (2\ell-1)!! \left[\frac{2\ell+1}{4\pi(\ell+m)!(\ell-m)!}\right]^{1/2} \times \sum_{k=0}^{m} i^{m-k} \frac{m!}{(m-k)!k!} \mathcal{A}_{[k,m-k,\ell-m]}(\Omega). \quad (55)$$

The Cartesian harmonics may be, on the other hand, expressed as

$$\mathcal{A}_{\vec{\ell}}(\Omega) = \sum_{m=-\ell}^{\ell} \left(a_{\vec{\ell}}^{m}\right)^* Y_{\ell m}(\Omega), \quad (56)$$

where [26] for $m \geqslant 0$,

$$a_{\vec{\ell}}^{m} = (-1)^m (2\ell-1)!! \left[\frac{2\ell+1}{4\pi(\ell+m)!(\ell-m)!}\right]^{1/2} \times \sum_{k=0}^{m} i^{m-k} \frac{m!}{(m-k)!k!} \langle \vec{\ell} | [k, m-k, \ell-m] \rangle, \quad (57)$$

the overlap integral $\langle \cdot | \cdot \rangle$ is given in Eq. (54), and $a_{\vec{\ell}}^{-m} = (-1)^m \left(a_{\vec{\ell}}^{m}\right)^*$. Formulas for conversion between tesseral and Cartesian harmonics for $\ell \leqslant 4$ are given in Table II.

Many circumstances require multiplication or division of the functions of spherical angle. For example, the empirical correlation function $C = 1 + \mathcal{R}$, as a function of spherical angle at a given $\boldsymbol{P}$ and q, follows from an equation of the form

$$X(\Omega) = C(\Omega) B(\Omega), \quad (58)$$

where the left-hand side represents the measured two-particle yield, $X(\Omega) \equiv \frac{d^6 N^{ab}}{d^3 p_a d^3 p_b}$, cf. Eq. (1), while B on the right-hand side is the product of single-particle yields, $\frac{dN^a}{d^3 p_a} \frac{dN^b}{d^3 p_b}$, and possibly of two-particle efficiency. To find $C(\Omega)$, one could bin the three functions in two dimensions of $\cos\theta$ and ϕ and obtain C within each bin by dividing the value of X in the bin by the value of B in the bin. However, if one next wanted to expand C in Cartesian harmonics, the result could be distorted by residual binning effects, which would disappear in the limit of fine binning but could only be afforded for high statistics. An alternative approach is to explicitly solve for the coefficients $C_{\vec{\ell}}$ given $X_{\vec{\ell}}$ and $B_{\vec{\ell}}$. With this, one could forego the binning in $\cos\theta$ and ϕ. For instance, when assessing X and identifying a particle pair at an angle Ω, one could increment values in an array for $X_{\vec{\ell}}$ by $[(2\ell+1)!!/\ell!]\mathcal{A}_{\vec{\ell}}(\Omega)$, as described by Eq. (9). One could then carry out an analogous procedure for the mixed pairs, filtering them through two-particle efficiency. In this way, both $X_{\vec{\ell}}$ and $B_{\vec{\ell}}$ could be obtained in a straightforward fashion, without any binning in $\cos\theta$ and ϕ.

Though the determination of $X_{\vec{\ell}}$ and $B_{\vec{\ell}}$ could be straightforward, the determination of $C_{\vec{\ell}}$ can be more difficult. Here, we outline one possible procedure based on the expansion (8) of the functions in powers of $\hat{q}$. If we introduce

$$\gamma(\vec{\ell}) = \frac{\ell!}{\ell_x!\ell_y!\ell_z!}, \quad (59)$$

we can write

$$X(\hat{q}) = \sum_{\vec{\ell}} \gamma(\vec{\ell}) X_{\vec{\ell}} \hat{q}_x^{\ell_x} \hat{q}_y^{\ell_y} \hat{q}_z^{\ell_z} = \sum_{\vec{\ell}} \sum_{\substack{\vec{\ell}' \\ 0 \leqslant \ell_i' \leqslant \ell_i}} \gamma(\vec{\ell}-\vec{\ell}')\gamma(\vec{\ell}') B_{\vec{\ell}-\vec{\ell}'} C_{\vec{\ell}'} \hat{q}_x^{\ell_x} \hat{q}_y^{\ell_y} \hat{q}_z^{\ell_z}. \quad (60)$$

If the condition of tracelessness for $\bar{C}_{\vec{\ell}}$ is lifted, the solution to Eq. (60) ceases to be unique, because $\hat{q}_i$ are not independent due to the constraint $\hat{q}_x^2 + \hat{q}_y^2 + \hat{q}_z^2 = 1$. We will first find a solution to Eq. (60) without imposing the tracelessness condition, which will provide us with $C(\Omega)$ from which we can next find the traceless $C_{\vec{\ell}}$.

The simplest strategy in finding a solution to Eq. (60) is to treat the components $\hat{q}_i$ as if they were independent. If we denote the solution by $\bar{C}_{\vec{\ell}}$, we obtain

$$\gamma(\vec{\ell}) X_{\vec{\ell}} = \sum_{\substack{\vec{\ell}' \\ 0 \leqslant \ell_i' \leqslant \ell_i}} \gamma(\vec{\ell}-\vec{\ell}')\gamma(\vec{\ell}') B_{\vec{\ell}-\vec{\ell}'} \bar{C}_{\vec{\ell}'}, \quad (61)$$

which may be solved for $\bar{C}_{\vec{\ell}}$ iteratively. The $\ell = 0$ term follows right away,

$$\bar{C}_0 = \frac{X_0}{B_0}, \quad (62)$$

while the subsequent coefficients follow from

$$\bar{C}_{\vec{\ell}} = \frac{X_{\vec{\ell}}}{B_{\vec{\ell}}} - \frac{1}{\gamma(\vec{\ell}) B_{\vec{\ell}}} \sum_{\substack{\vec{\ell}' \\ \ell' \leqslant \ell-1 \\ 0 \leqslant \ell_i' \leqslant \ell_i}} \gamma(\vec{\ell}-\vec{\ell}')\gamma(\vec{\ell}') B_{\vec{\ell}-\vec{\ell}'} \bar{C}_{\vec{\ell}'}. \quad (63)$$

The combination of

$$C(\Omega) = \sum_{\vec{\ell}} \gamma(\vec{\ell}) \bar{C}_{\vec{\ell}} \hat{q}_x^{\ell_x} \hat{q}_y^{\ell_y} \hat{q}_z^{\ell_z}, \quad (64)$$

and of Eq. (9) next yields for the traceless coefficients

$$C_{\vec{\ell}} = \frac{(2\ell+1)!!}{\ell!} \int \frac{d\Omega}{4\pi} \mathcal{A}_{\vec{\ell}}(\Omega) C(\Omega) = \frac{(2\ell+1)!!}{\ell!} \sum_{\vec{m}} \gamma(\vec{\ell}+2\vec{m}) \langle \vec{\ell} | \vec{\ell}+2\vec{m}] \bar{C}_{\vec{\ell}+2\vec{m}}, \quad (65)$$

with

$$\langle \vec{\ell} | \vec{\ell}'] \equiv \int \frac{d\Omega}{4\pi} \mathcal{A}_{\vec{\ell}}(\Omega) \hat{n}_x^{\ell_x'} \hat{n}_y^{\ell_y'} \hat{n}_z^{\ell_z'} = \frac{(2\ell+1)!!}{(\ell+\ell'+1)!!} \times \sum_{\substack{\vec{m} \\ 0 \leqslant m_i \leqslant \ell'/2 \\ m=(\ell'-\ell)/2}} \frac{1}{2^m} \frac{\ell_x'!}{(\ell_x'-2m_x)!m_x!} \frac{\ell_y'!}{(\ell_y'-2m_y)!m_y!} \times \frac{\ell_z'!}{(\ell_z'-2m_z)!m_z!} \langle \vec{\ell} | \vec{\ell}' - 2\vec{m} \rangle, \quad (66)$$

where in the second equality, we made use of the expansion (52) for the product of direction vector components.

In practical circumstances, the sums over ℓ must be cut off at some $\ell_{\max}$. This is because, on one hand, the experimental apparatus and the statistics limit the angular resolution and, on the other, the features of a reaction limit the number of ℓ for which $C_{\vec{\ell}}$ may be significant. Exceeding a sensible

TABLE II. Transformation equations between Cartesian and tesseral harmonics for $\ell \leqslant 4$.

$$Y_{10} = (1/2)\sqrt{3/\pi}\,\mathcal{A}^{(1)}_{z}$$
$$Y_{1\pm1} = -(i/2)\sqrt{3/2\pi}\,\mathcal{A}^{(1)}_{y} \mp (1/2)\sqrt{3/2\pi}\,\mathcal{A}^{(1)}_{x}$$
$$Y_{20} = (3/4)\sqrt{5/\pi}\,\mathcal{A}^{(2)}_{zz}$$
$$Y_{2\pm1} = -(i/2)\sqrt{15/2\pi}\,\mathcal{A}^{(2)}_{yz} \mp (1/2)\sqrt{15/2\pi}\,\mathcal{A}^{(2)}_{xz}$$
$$Y_{2\pm2} = -(1/4)\sqrt{15/2\pi}\,\mathcal{A}^{(2)}_{yy} \pm (i/2)\sqrt{15/2\pi}\,\mathcal{A}^{(2)}_{xy} + (1/4)\sqrt{15/2\pi}\,\mathcal{A}^{(2)}_{xx}$$
$$Y_{30} = (5/4)\sqrt{7/\pi}\,\mathcal{A}^{(3)}_{zzz}$$
$$Y_{3\pm1} = -(5i/8)\sqrt{21/\pi}\,\mathcal{A}^{(3)}_{yzz} \mp (5/8)\sqrt{21/\pi}\,\mathcal{A}^{(3)}_{xzz}$$
$$Y_{3\pm2} = -(1/4)\sqrt{105/2\pi}\,\mathcal{A}^{(3)}_{yyz} \pm (i/2)\sqrt{105/2\pi}\,\mathcal{A}^{(3)}_{xyz} + (1/4)\sqrt{105/2\pi}\,\mathcal{A}^{(3)}_{xxz}$$
$$Y_{3\pm3} = (i/8)\sqrt{35/\pi}\,\mathcal{A}^{(3)}_{yyy} \pm (3/8)\sqrt{35/\pi}\,\mathcal{A}^{(3)}_{xyy} - (3i/8)\sqrt{35/\pi}\,\mathcal{A}^{(3)}_{xxy} \mp (1/8)\sqrt{35/\pi}\,\mathcal{A}^{(3)}_{xxx}$$
$$Y_{40} = (105/16)\sqrt{1/\pi}\,\mathcal{A}^{(4)}_{zzzz}$$
$$Y_{4\pm1} = -(21i/8)\sqrt{5/\pi}\,\mathcal{A}^{(4)}_{yzzz} \mp (21/8)\sqrt{5/\pi}\,\mathcal{A}^{(4)}_{xzzz}$$
$$Y_{4\pm2} = -(21/8)\sqrt{5/2\pi}\,\mathcal{A}^{(4)}_{yyzz} \pm (21i/4)\sqrt{5/2\pi}\,\mathcal{A}^{(4)}_{xyzz} + (21/8)\sqrt{5/2\pi}\,\mathcal{A}^{(4)}_{xxzz}$$
$$Y_{4\pm3} = (3i/8)\sqrt{35/\pi}\,\mathcal{A}^{(4)}_{yyyz} \pm (9/8)\sqrt{35/\pi}\,\mathcal{A}^{(4)}_{xyyz} - (9i/8)\sqrt{35/\pi}\,\mathcal{A}^{(4)}_{xxyz} \mp (3/8)\sqrt{35/\pi}\,\mathcal{A}^{(4)}_{xxxz}$$
$$Y_{4\pm4} = (3/16)\sqrt{35/2\pi}\,\mathcal{A}^{(4)}_{yyyy} \mp (3i/4)\sqrt{35/2\pi}\,\mathcal{A}^{(4)}_{xyyy} - (9/8)\sqrt{35/2\pi}\,\mathcal{A}^{(4)}_{xxyy} \pm (3i/4)\sqrt{35/2\pi}\,\mathcal{A}^{(4)}_{xxxy} + (3/16)\sqrt{35/2\pi}\,\mathcal{A}^{(4)}_{xxxx}$$

$$\mathcal{A}^{(1)}_{z} = 2\sqrt{\pi/3}\,Y_{10}$$
$$\mathcal{A}^{(1)}_{y} = i\sqrt{2\pi/3}\,Y_{11} + i\sqrt{2\pi/3}\,Y_{1-1}$$
$$\mathcal{A}^{(1)}_{x} = -\sqrt{2\pi/3}\,Y_{11} + \sqrt{2\pi/3}\,Y_{1-1}$$
$$\mathcal{A}^{(2)}_{zz} = (4/3)\sqrt{\pi/5}\,Y_{20}$$
$$\mathcal{A}^{(2)}_{yz} = i\sqrt{2\pi/15}\,Y_{21} + i\sqrt{2\pi/15}\,Y_{2-1}$$
$$\mathcal{A}^{(2)}_{yy} = -\sqrt{2\pi/15}\,Y_{22} - (2/3)\sqrt{\pi/5}\,Y_{20} - \sqrt{2\pi/15}\,Y_{2-2}$$
$$\mathcal{A}^{(2)}_{xz} = -\sqrt{2\pi/15}\,Y_{21} + \sqrt{2\pi/15}\,Y_{2-1}$$
$$\mathcal{A}^{(2)}_{xy} = -i\sqrt{2\pi/15}\,Y_{22} + i\sqrt{2\pi/15}\,Y_{2-2}$$
$$\mathcal{A}^{(2)}_{xx} = \sqrt{2\pi/15}\,Y_{22} - (2/3)\sqrt{\pi/5}\,Y_{20} + \sqrt{2\pi/15}\,Y_{2-2}$$
$$\mathcal{A}^{(3)}_{zzz} = (4/5)\sqrt{\pi/7}\,Y_{30}$$
$$\mathcal{A}^{(3)}_{yzz} = (4i/5)\sqrt{\pi/21}\,Y_{31} + (4i/5)\sqrt{\pi/21}\,Y_{3-1}$$
$$\mathcal{A}^{(3)}_{yyz} = -\sqrt{2\pi/105}\,Y_{32} - (2/5)\sqrt{\pi/7}\,Y_{30} - \sqrt{2\pi/105}\,Y_{3-2}$$
$$\mathcal{A}^{(3)}_{yyy} = -i\sqrt{\pi/35}\,Y_{33} - (i/5)\sqrt{3\pi/7}\,Y_{31} - (i/5)\sqrt{3\pi/7}\,Y_{3-1} - i\sqrt{\pi/35}\,Y_{3-3}$$
$$\mathcal{A}^{(3)}_{xzz} = -(4/5)\sqrt{\pi/21}\,Y_{31} + (4/5)\sqrt{\pi/21}\,Y_{3-1}$$
$$\mathcal{A}^{(3)}_{xyz} = -i\sqrt{2\pi/105}\,Y_{32} + i\sqrt{2\pi/105}\,Y_{3-2}$$
$$\mathcal{A}^{(3)}_{xyy} = \sqrt{\pi/35}\,Y_{33} + (1/5)\sqrt{\pi/21}\,Y_{31} - (1/5)\sqrt{\pi/21}\,Y_{3-1} - \sqrt{\pi/35}\,Y_{3-3}$$
$$\mathcal{A}^{(3)}_{xxz} = \sqrt{2\pi/105}\,Y_{32} - (2/5)\sqrt{\pi/7}\,Y_{30} + \sqrt{2\pi/105}\,Y_{3-2}$$
$$\mathcal{A}^{(3)}_{xxy} = i\sqrt{\pi/35}\,Y_{33} - (i/5)\sqrt{\pi/21}\,Y_{31} - (i/5)\sqrt{\pi/21}\,Y_{3-1} + i\sqrt{\pi/35}\,Y_{3-3}$$
$$\mathcal{A}^{(3)}_{xxx} = -\sqrt{\pi/35}\,Y_{33} + (1/5)\sqrt{3\pi/7}\,Y_{31} - (1/5)\sqrt{3\pi/7}\,Y_{3-1} + \sqrt{\pi/35}\,Y_{3-3}$$
$$\mathcal{A}^{(4)}_{zzzz} = (16/105)\sqrt{\pi}\,Y_{40}$$
$$\mathcal{A}^{(4)}_{yzzz} = (4i/21)\sqrt{\pi/5}\,Y_{41} + (4i/21)\sqrt{\pi/5}\,Y_{4-1}$$
$$\mathcal{A}^{(4)}_{yyzz} = -(2/21)\sqrt{2\pi/5}\,Y_{42} - (8/105)\sqrt{\pi}\,Y_{40} - (2/21)\sqrt{2\pi/5}\,Y_{4-2}$$
$$\mathcal{A}^{(4)}_{yyyz} = -(i/3)\sqrt{\pi/35}\,Y_{43} - (i/7)\sqrt{\pi/5}\,Y_{41} - (i/7)\sqrt{\pi/5}\,Y_{4-1} - (i/3)\sqrt{\pi/35}\,Y_{4-3}$$
$$\mathcal{A}^{(4)}_{yyyy} = (1/3)\sqrt{2\pi/35}\,Y_{44} + (2/21)\sqrt{2\pi/5}\,Y_{42} + (2/35)\sqrt{\pi}\,Y_{40} + (2/21)\sqrt{2\pi/5}\,Y_{4-2} + (1/3)\sqrt{2\pi/35}\,Y_{4-4}$$
$$\mathcal{A}^{(4)}_{xzzz} = -(4/21)\sqrt{\pi/5}\,Y_{41} + (4/21)\sqrt{\pi/5}\,Y_{4-1}$$
$$\mathcal{A}^{(4)}_{xyzz} = -(2i/21)\sqrt{2\pi/5}\,Y_{42} + (2i/21)\sqrt{2\pi/5}\,Y_{4-2}$$
$$\mathcal{A}^{(4)}_{xyyz} = (1/3)\sqrt{\pi/35}\,Y_{43} + (1/21)\sqrt{\pi/5}\,Y_{41} - (1/21)\sqrt{\pi/5}\,Y_{4-1} - (1/3)\sqrt{\pi/35}\,Y_{4-3}$$
$$\mathcal{A}^{(4)}_{xyyy} = (i/3)\sqrt{2\pi/35}\,Y_{44} + (i/21)\sqrt{2\pi/5}\,Y_{42} - (i/21)\sqrt{2\pi/5}\,Y_{4-2} - (i/3)\sqrt{2\pi/35}\,Y_{4-4}$$
$$\mathcal{A}^{(4)}_{xxzz} = (2/21)\sqrt{2\pi/5}\,Y_{42} - (8/105)\sqrt{\pi}\,Y_{40} + (2/21)\sqrt{2\pi/5}\,Y_{4-2}$$
$$\mathcal{A}^{(4)}_{xxyz} = (i/3)\sqrt{\pi/35}\,Y_{43} - (i/21)\sqrt{\pi/5}\,Y_{41} - (i/21)\sqrt{\pi/5}\,Y_{4-1} + (i/3)\sqrt{\pi/35}\,Y_{4-3}$$
$$\mathcal{A}^{(4)}_{xxyy} = -(1/3)\sqrt{2\pi/35}\,Y_{44} + (2/105)\sqrt{\pi}\,Y_{40} - (1/3)\sqrt{2\pi/35}\,Y_{4-4}$$
$$\mathcal{A}^{(4)}_{xxxz} = -(1/3)\sqrt{\pi/35}\,Y_{43} + (1/7)\sqrt{\pi/5}\,Y_{41} - (1/7)\sqrt{\pi/5}\,Y_{4-1} + (1/3)\sqrt{\pi/35}\,Y_{4-3}$$
$$\mathcal{A}^{(4)}_{xxxy} = -(i/3)\sqrt{2\pi/35}\,Y_{44} + (i/21)\sqrt{2\pi/5}\,Y_{42} - (i/21)\sqrt{2\pi/5}\,Y_{4-2} + (i/3)\sqrt{2\pi/35}\,Y_{4-4}$$
$$\mathcal{A}^{(4)}_{xxxx} = (1/3)\sqrt{2\pi/35}\,Y_{44} - (2/21)\sqrt{2\pi/5}\,Y_{42} + (2/35)\sqrt{\pi}\,Y_{40} - (2/21)\sqrt{2\pi/5}\,Y_{4-2} + (1/3)\sqrt{2\pi/35}\,Y_{4-4}$$

$\ell_{\max}$ will result in coefficients dominated by noise. A likely situation is that of a suitable value of $\ell_{\max}$ higher for X, B, and $\bar{C}$ than for C. This is because the anisotropies associated with measurement efficiencies, particularly at small q, can be much stronger than physical anisotropies, especially when the experiment is blind in certain directions. In the latter case, the binning method would necessarily fail for small bins, while the method relying on the $\vec{\ell}$ decomposition from the start could succeed when using large $\ell_{\max}$ for X and B, as long as only low ℓ values were demanded of C.

Strategies similar to that employed for finding C in Eq. (58) may be employed for finding the expansion coefficients for an inverse of an angular function or for a product of angular functions. In finding the inverse of B in terms of $B_{\vec{\ell}}$, one would replace $X(\Omega)$ in Eq. (58) by 1, leading to $X_{\vec{\ell}} = \delta_{\ell 0}$ in Eqs. (62) and (63). On the other hand, in looking for the product of B and C in terms of expansion coefficients, one can first obtain the coefficients

$$\bar{X}_{\vec{\ell}} = \frac{1}{\gamma(\vec{\ell})} \sum_{\substack{\vec{\ell}' \\ 0 \leqslant \ell'_i \leqslant \ell_i}} \gamma(\vec{\ell} - \vec{\ell}')\gamma(\vec{\ell}')B_{\vec{\ell}-\vec{\ell}'}C_{\vec{\ell}'}, \tag{67}$$

which do not meet the condition of tracelessness. Next, one can obtain traceless coefficients $X_{\vec{\ell}}$ following such a procedure as for C in Eqs. (65)–(66). Obviously, that specific detracing procedure is a form of application of the projection operator $\mathcal{P}$, described in the Appendix, to a symmetric tensor.

We have thus demonstrated some practical procedures for dividing, inverting, and multiplying angular functions in terms of $\vec{\ell}$ arrays without resorting to binning of the functions in $\cos\theta$ or $\cos\phi$ and without performing matrix inversion operations.

IV. PRACTICAL ASPECTS OF SHAPE ANALYSIS

The expansion of correlations and sources in tesseral or Cartesian harmonics brings about practical benefits. The three-dimensional dependencies on relative momentum and spatial separation of the functions are replaced by sets of one-dimensional dependencies of angular expansion coefficients. The replacement of the three-dimensional by one-dimensional dependencies principally allows a more thorough representation of the correlation data and of the physical picture of those data's implications. The three-dimensional integral relation between the correlation function and source gets replaced by a set of one-dimensional relations between the respective expansion coefficients, simplifying the task of finding the source features. The expansion coefficients for the functions, as either spherical or Cartesian tensors, transform covariantly under rotations.

Of the two sets of harmonic functions for expansion, the tesseral set represents an orthonormal basis but leads to coefficients which are complex and hard to interpret. On the other hand, the Cartesian set is overcomplete and generally nonorthogonal within any rank, but it yields real coefficients with relatively straightforward interpretations. The transformation properties under rotations are more straightforward for the Cartesian than for the tesseral coefficients. We have shown, in the preceding section, how to transcribe results between the two harmonic representations.

A. Shapes in terms of Cartesian harmonics

Along any direction of relative momentum or separation, the correlation or source function is equal to combinations of the Cartesian coefficients [Eq. (8)]. Particularly simple results follow along any of the employed Cartesian axes; e.g., along the positive direction for the x axis the correlation function is

$$\mathcal{R}(q) = \mathcal{R}^{(0)}(q) + \mathcal{R}^{(1)}_x(q) + \mathcal{R}^{(2)}_{xx}(q) + \mathcal{R}^{(3)}_{xxx}(q) + \cdots. \tag{68}$$

Terms for subsequent ℓ refine the information on the dependence of the function on q, along the direction. As we have mentioned, the physics on the one hand and statistics and apparatus on the other will limit the number of significant terms in the expansion, with the high-ℓ terms being dominated by noise [24].

For identical particles, the correlation function and accessed emission source are invariant under inversion. In such a case, the odd-ℓ terms in the harmonic expansion vanish. That is generally not the case for nonidentical particles. For instance, if the protons in a reaction are, on the average, emitted earlier than pions, the distribution $\mathcal{S}$ of pairs in $\boldsymbol{r}_p - \boldsymbol{r}_\pi$ will be pushed out in the outward direction, away from 0. The three $\ell = 1$ Cartesian moments in Eq. (52), computed from $\mathcal{S}^{(1)}_\alpha$, yield the magnitude and precise direction of the average displacement of the distribution. At individual r, the effects onto $\mathcal{S}$ of different emission times and possibly different emission locations will result in a dipole distortion representable in terms of magnitude and direction as

$$\mathcal{S}^{(1)}_\alpha(r) = S^{(1)}(r)e^{(1)}_\alpha(r). \tag{69}$$

In the above, the direction vector is $\boldsymbol{e}^{(1)} = [\sin\theta^{(1)}\cos\phi^{(1)}, \sin\theta^{(1)}\sin\phi^{(1)}, \cos\theta^{(1)}]$. Not only the magnitude of the angular distortion but also the characteristic directions of the distortion can depend on the relative distance. If the distortion direction is independent of the distance, this direction will be the same for the average displacement and for the correlation at any relative momentum. The latter occurs because the kernel $\mathcal{K}_\ell$ is universal within a given rank, i.e., the same for different tensor components. The $\ell = 1$ distortions are behind the effects investigated by Gelderloos *et al.* [32] and Lednicky *et al.* [33], who compared pair emission probabilities for pairs with relative momenta directed along and opposite to the pair total momentum. The advantage of using the Cartesian harmonics is the ability to determine the distortion directions in correlation, and the implication of those distortions for source distortions, without any presumption regarding the distortion direction when no possible symmetry arguments can be invoked.

Quadratic moments of the emission source are associated with the rank $\ell = 2$ and $\ell = 0$ expansion coefficients, cf. Eq. (53), with the $\ell = 2$ rank giving rise to an anisotropy of the tensor out of the moments $\langle r_{\alpha_1} r_{\alpha_2}\rangle$. A triaxial ellipsoid could be associated with those moments, with Euler angles describing rotation from the coordinate axes to the axes of the ellipsoid, i.e., the axes along which the tensor of moments

gets diagonalized. At any value of the corresponding relative variable, for either the source or the correlation function, the rank $\ell = 2$ symmetric and traceless tensor of expansion coefficients may be diagonalized and described in terms of five independent parameters, two distortions and three angles:

$$\mathcal{S}^{(2)}_{\alpha_1\alpha_2}(r) = S^{(2)}_1 e^{(2)}_{1\alpha_1} e^{(2)}_{1\alpha_2} - \left(S^{(2)}_1 + S^{(2)}_3\right) e^{(2)}_{2\alpha_1} e^{(2)}_{2\alpha_2} + S^{(2)}_3 e^{(2)}_{3\alpha_1} e^{(2)}_{3\alpha_2}. \quad (70)$$

The three eigenvectors $\boldsymbol{e}^{(2)}_i$ in Eq. (70) form an orthonormal set. Because of the tracelessness of $\mathcal{S}^{(2)}$, the distortions associated with the three directions add up to zero, $S^{(2)}_2 = -(S^{(2)}_1 + S^{(2)}_3)$. In terms of the Euler angles $\Phi^{(2)}$, $\Theta^{(2)}$, and $\Psi^{(2)}$, for rotation of unit vectors along coordinate axes to $\{\boldsymbol{e}^{(2)}_i\}_{i=1,2,3}$, the eigenvectors may be represented as

$$\begin{aligned}
\boldsymbol{e}_1 &= [\cos\Psi\cos\Phi - \cos\Theta\sin\Psi\sin\Phi, \cos\Psi\sin\Phi \\
&\quad + \cos\Theta\cos\Psi\sin\Phi, \sin\Psi\sin\Theta], \\
\boldsymbol{e}_2 &= [-\sin\Psi\cos\Phi - \cos\Theta\sin\Psi\cos\Phi, -\sin\Psi\sin\Phi \\
&\quad + \cos\Theta\cos\Psi\cos\Phi, \cos\Psi\sin\Theta], \\
\boldsymbol{e}_3 &= [\sin\Theta\sin\Phi, -\sin\Theta\cos\Phi, \cos\Theta], \qquad (71)
\end{aligned}$$

where the (2) superscripts are suppressed. Just as the distortion values, the angles may depend on r. If the angles do not depend on r, then those angles coincide with those for the diagonalization of the tensor of quadratic moments $\langle r_{\alpha_1} r_{\alpha_2}\rangle$ and for the diagonalization of the quadrupole coefficients of the correlation function at any q. The five independent parameters at any relative variable correspond to five independent expansion coefficients for rank $\ell = 2$.

With regard to the higher, $\ell > 2$, shape distortions, one way to associate the directions of axes with them is to choose one direction, defined by $\boldsymbol{e}^{(\ell)}_1$, by demanding that the distortion along that direction, equal to

$$S^{(\ell)}(\Omega) = \sum_{\alpha_1\ldots\alpha_\ell} \mathcal{S}^{(\ell)}_{\alpha_1\ldots\alpha_\ell} e^{(\ell)}_{1\alpha_1}\ldots e^{(\ell)}_{1\alpha_\ell}, \qquad (72)$$

is extremal, minimal or maximal [25]. Directing a coordinate axis along $\boldsymbol{e}^{(\ell)}_1$, makes the two $\mathcal{S}^{(\ell)}$ coefficients, characterized by $\ell_1 = \ell - 1$, vanish. The next axis, defined by $\boldsymbol{e}^{(\ell)}_2$, may be chosen again as one extremizing the distortion, but now within the direction plane perpendicular to $\boldsymbol{e}^{(\ell)}_1$. When directing the second coordinate axis along $\boldsymbol{e}^{(\ell)}_2$ and the third along the direction perpendicular to the first two, we find that the choice puts to zero the $\mathcal{S}^{(\ell)}$ coefficient characterized by $\ell_1 = 0$, $\ell_2 = \ell - 1$, and $\ell_3 = 1$.

B. Harmonic decomposition vs fits in three dimensions

For a given total momentum, the correlation function contains three-dimensional information pertinent to the three-dimensional structure of the source function. Effectively, there are three competing approaches for handling the information in the correlation function. The first approach, most common till now in literature, presents the data along chosen discrete directions of relative momentum, typically one or three. The second approach fits the data to a parametrized form, e.g., a three-dimensional Gaussian, in the full three-dimensional space of relative momentum. When going beyond the simplest parametrizations in this approach, it may be difficult to assess, working in the three-dimensional space, which aspects of the source parametrization affect which particular aspects of the correlation. The third approach expands the data in harmonic functions. A set of one-dimensional functions then yields a complete representation of the three-dimensional data. Upon decomposition, the deduction of source features is reduced to a set of one-dimensional problems, with one-to-one correspondence between the coefficients of the correlation and the source. A specific coefficient of the source affects the specific coefficient of the correlation function and no other independent coefficients. Whether one advances the source analysis as an inversion problem or as a problem of fitting, it should be certainly preferable to divide and conquer, i.e., approach the issue as a set one-dimensional problems.

Spherical harmonic decompositions generally carry more information than can be expressed with parameters of Gaussian sources employed in the literature. The integrated nine independent source coefficients $\mathcal{S}^{(\ell)}$ for $\ell \leqslant 2$ fully determine the moments $\langle r_{\alpha_1} r_{\alpha_2}\rangle$ and $\langle r_\alpha\rangle$, for all α indices, cf. Eq. (52). Those moments and the integral of $S^{(0)}$, $\lambda = 4\pi \int dr r^2 \mathcal{S}^{(0)}(r)$, determine all 10 parameters that can be set for a Gaussian source such as discussed in Ref. [25] or in the next section. However, the coefficients $\mathcal{S}^{(\ell)}$ for $\ell \leqslant 2$ may have a different dependence on r than those for a Gaussian source. In addition, the $\ell > 2$ coefficients may further yield different characteristic moments. When coordinate axes are directed along the principal axes of the Gaussian quadrupole deformation, the Gaussian moments, relative to Gaussian center, factorize:

$$\begin{aligned}
&\langle (r_1 - \langle r_1\rangle)^{\ell_1} (r_2 - \langle r_2\rangle)^{\ell_2} (r_3 - \langle r_3\rangle)^{\ell_3}\rangle \\
&\quad = \langle (r_1 - \langle r_1\rangle)^{\ell_1}\rangle \langle (r_2 - \langle r_2\rangle)^{\ell_2}\rangle \langle (r_3 - \langle r_3\rangle)^{\ell_3}\rangle. \qquad (73)
\end{aligned}$$

For distinguishable particles in the midrapidity region of symmetric ultrarelativistic collisions, the above implies that $\langle r_{\rm out} r^2_{\rm long}\rangle = \langle r_{\rm out}\rangle \langle r^2_{\rm long}\rangle$. The latter factorization will be violated, for instance, for boost-invariant particle emission, such as discussed in Sec. V B. In the case of boost-invariant emission, with a transverse expansion, the single-particle sources acquire a boomerang-type shape, as particles at lower positions along the beam axis get emitted locally earlier than particles at higher positions. The violation of the factorization above will become apparent if one, e.g., observes that the boomerang shape will be preserved in the relative source when one of the emitted particles is heavy (baryon) and the other light (π meson). Features of a boomerang shape may be quantified with the source expansion coefficients for $\ell = 3$, which contribute to the moment $\langle r_{\rm out} r^2_{\rm long}\rangle$, cf. Eq. (52), which may be compared to the product $\langle r_{\rm out}\rangle \langle r^2_{\rm long}\rangle$ from $\ell = 1$ and $\ell = 2$, besides $\ell = 0$.

With regard to the dependence of $\mathcal{S}^{(\ell)}$ on r, several studies have already focused on determining the non-Gaussian behavior of the angle-averaged source function, $\mathcal{S}^{(\ell=0)}(r)$. With regard to $\ell \geqslant 1$, significant values of $\mathcal{S}^{(\ell)}(r)$ are principally expected only where $\mathcal{S}^{(\ell=0)}(r)$ begins to fall, i.e., around the edges of the source; whereas at small r, $\mathcal{S}^{(\ell)}(r) \propto r^\ell$. Concerning the low-$r$ region, in the source-correlation relation,

the convolution with kernel $\mathcal{K}_\ell$ brings in a factor r^2. That low-r suppression generally reduces the impact of small-r $S^{(\ell)}$ on the correlation, enhancing errors in the restored source and making it likely difficult to detect any non-Gaussian features there at $\ell \geqslant 1$. On the other hand, in the source tails at $\ell \geqslant 1$ in the source coefficients, the non-Gaussian behavior may be actually enhanced compared to $\ell = 0$, both at low and high reaction energies. For instance, long-lived slowly cooling systems with emission rates falling off as $\exp(-t/\tau)$ should give rise to relative sources with an exponential falloff along the direction that the pair total momentum has in the frame of the emitting system. For low ℓ, strength of the exponential tail should increase with (ℓ) for distortion along the direction of the total momentum, Eq. (72). In fact, looking for the maximal distortion in source tail may help locate the emitting source within the velocity space. In ultrarelativistic collisions, the emission becomes boost invariant around the midrapidity. For a freezing-out boost-invariant thermal source, the single-particle distribution of emission points in the space-time, cf. Eq. (2), has the form

$$s(\boldsymbol{p}, \boldsymbol{r}, t) \sim \delta(\tau - \tau_f)\exp(-E_\perp\sqrt{1 + z^2/\tau^2}/T), \quad (74)$$

where $\tau = \sqrt{t^2 - z^2}$ and z points along the beam axis. The single-particle source above falls off exponentially with an increase in $|z|$ and so would the relative source with an increase in $|r_{\rm long}|$. This behavior should be particularly revealed in the $\mathcal{S}_{[0,0,2k]}$ coefficients of the relative source.

While it may be straightforward to compute the expansion coefficients as convolutions of the correlation with different harmonics, some caution should be exerted in selecting the range of relative momentum q for the source investigation. The caution is required because there exist other causes for interparticle correlation than the final-state effects within a two-particle system. At the mathematical level, those causes can give rise to a $\boldsymbol{q}$ dependence of the source $\mathcal{S}$, assumed to be negligible in arriving at Eq. (1). The dependence might be produced by a collective expansion of strength comparable to or larger than the local thermal motion in the emitting region. If the dependence is not explicitly corrected for, the analysis for source restoration should be limited to the region where the source $\boldsymbol{q}$ dependence is deemed weak. In the case of the final-state effects due to resonances, short distances in $\mathcal{S}$ are important, with the q dependence governed there by local temperature at freeze-out, giving rise to the requirement of $q \ll \sqrt{2\mu T}$ for the source analysis. This condition is practically always satisfied for pp pairs whose correlation function peaks at $q \sim 20$ MeV/c. On the other hand, for $p\pi^+$ pairs in the region of Δ resonance at $q \sim 225$ MeV/c, the condition is practically never satisfied in nuclear reactions. Correlations due to directed flow associated with the reaction plane, such as elliptic and sideward flows, can be partially accounted for by controlling the reaction plane in constructing the denominator in Eq. (1). Otherwise, that type of correlation tends to peak at q of the order of the mean $p_\perp$ (i.e., a few hundred MeV/c for p or π in energetic collisions), reaching there values of the order of a few percent. By comparison, Coulomb correlations fall off with increase of q, as $1/q^2$, down to about 1% for pp typically at $q \sim 100$ MeV/c. That further underscores the need to limit the range of q in source analysis. In ultrarelativistic collisions, jets are an additional cause for interparticle correlations. The characteristic scale for those correlations is of the order of several hundred MeV/c and the magnitude of the order of 1% toward lower $p_\perp$. Overall, it is apparent that caution should be executed when considering small values of the $\mathcal{R}$, i.e., of the order of half a percent or less. If conclusions are to hinge on such small values, some supporting evidence should be provided to justify the assumption that the correlation originates from final-state interactions or symmetrization.

V. EXAMPLES OF EMISSION

Here, we provide examples of what may be expected in reactions regarding harmonic characterization of emission sources and correlation functions.

A. Gaussian sources

In the analyses of correlation functions, it is quite common to aim at a Gaussian representation of the emission sources. When cast in the Gaussian form, a source is expressed in terms of a minimal number of parameters needed for shape description.

Thus, a Gaussian source is generally described in terms of nine parameters, of which three describe the position of the source center $\boldsymbol{d}$ and six correspond to the independent independent matrix elements of the symmetric positive shape matrix M:

$$\mathcal{S}(\boldsymbol{r}) = \frac{[\det M]^{1/2}}{(4\pi)^{3/2}} \exp\left\{-\frac{1}{4}\sum_{\alpha_1\alpha_2} M_{\alpha_1\alpha_2}(r_{\alpha_1} - d_{\alpha_1})(r_{\alpha_2} - d_{\alpha_2})\right\}. \quad (75)$$

A tenth parameter would describe the normalization of the source, which could vary from unity if a significant fraction of the pairs had effectively infinite separations due to weak decays and were outside the description in terms of a single Gaussian. For identical particles, the accessed relative source must be symmetric under inversion, representing particle interchange. In that case $\boldsymbol{d} = 0$, leaving only six independent shape parameters for the source.

The convenient choice for the shape parameters are three Euler angles describing an orientation of the eigenvectors $\{\boldsymbol{u}_i\}$ of M and three Gaussian radii R_i in terms of which the matrix is $M_{\alpha_1\alpha_2} = \sum_i (1/R_i^2)\boldsymbol{u}_{i\alpha_1}\boldsymbol{u}_{i\alpha_2}$. The specific factor of $(1/4)$ multiplying M and $(1/R^2)$ in Eq. (75) is associated with the tradition of assigning the radii to the single-particle sources s in Eq. (2). However, absolute positions in a reaction are not observable; more appropriate for the description of relative positions would be a factor of $(1/2)$ yielding radii larger by a factor of $\sqrt{2}$. When coordinate axes are oriented along the Gaussian shape eigenvectors, the Gaussian shape takes the

form

$$\mathcal{S}(\boldsymbol{r}) = \frac{1}{(4\pi)^{3/2} R_x R_y R_z} \exp\left\{ -\frac{(x-d_x)^2}{4R_x^2} - \frac{(y-d_y)^2}{4R_y^2} - \frac{(z-d_z)^2}{4R_z^2} \right\}. \tag{76}$$

The displacement $\boldsymbol{d}$ of the source for distinguishable particles, relative to $\boldsymbol{r} = 0$, is of interest in both intermediate- and high-energy collisions [33,34]. For instance, at low energy, it might be of interest whether neutron emission preceded proton emission [35], producing a $\boldsymbol{d}$ in the direction of pair total momentum, or whether intermediate-mass fragments were emitted simultaneously with the protons [32]. At high energy, one might look for evidence of strange particles leaving early [36]. A simultaneous emission combined with radial expansion should lead to heavy-particle emission shifted out in the direction of expansion relative to light-particle emission [37].

In many circumstances, the structure of anisotropies for measured correlation functions and the corresponding structure for imaged sources simplify. Thus, if the reaction plane is not identified, the measured correlation function and the corresponding source must obey reflection symmetry with respect to the plane formed by the pair total momentum $\boldsymbol{P}$ and the beam axis. In the Gaussian representation, the displacement vector $\boldsymbol{d}$ must lie within that plane and so must two of the eigenvectors of the Gaussian shape matrix M. In the midrapidity region of a symmetric system, the correlation function and source must be moreover symmetric with respect to forward-backward reflection. That makes the $\boldsymbol{d}$ vector perpendicular to the beam axis and makes the in-plane Gaussian-shape eigenvectors pointing along and perpendicular to the beam axis [3].

The nine Gaussian parameters discussed above may be related to the angular moments of both the source and the correlation function. It may be tempting, in particular, to associate the three independent $\ell = 1$ moments with the displacement $\boldsymbol{d}$ and the five $\ell = 2$ moments with the shape anisotropy of a Gaussian. However, the situation is more involved. For illustration, one can consider an isotropic Gaussian displaced in the x direction, that is,

$$\begin{aligned}
\mathcal{S}(\boldsymbol{r}) &= \frac{1}{(4\pi)^{3/2} R^3} \exp\left\{ -\frac{(x-d)^2 + y^2 + z^2}{4R^2} \right\} \\
&= \frac{1}{(4\pi)^{3/2} R^3} \exp\left\{ -\frac{r^2 + d^2}{4R^2} \right\} \exp\left\{ \frac{xd}{2R^2} \right\} \\
&= \frac{1}{(4\pi)^{3/2} R^3} \exp\left\{ -\frac{r^2 + d^2}{4R^2} \right\} \\
&\quad \times \sum_{\ell=0}^{\infty} (2\ell+1) I_\ell\left(\frac{rd}{2R^2} \right) P_\ell(n_x) \\
&= \frac{1}{(4\pi)^{3/2} R^3} \exp\left\{ -\frac{r^2 + d^2}{4R^2} \right\} \\
&\quad \times \sum_{\ell=0}^{\infty} \frac{(2\ell+1)!!}{\ell!} I_\ell\left(\frac{rd}{2R^2} \right) \mathcal{A}^{(\ell)}_{xx\ldots x}(\Omega).
\end{aligned} \tag{77}$$

Here, I_ℓ are the modified spherical Bessel functions of the first kind. For small argument values of those functions, the functions are proportional to the power of the argument, $I_\ell(x) \propto x^\ell$. Equation (77) illustrates that the source displacement $\boldsymbol{d}$ produces nonzero angular moments for all $\ell \geqslant 1$ even when the Gaussian source is isotropic around its center. Incidentally, in a similar manner, for $\boldsymbol{d} = 0$, the anisotropy of a Gaussian gives rise to nonzero angular moments for all even $\ell \geqslant 2$, not just $\ell = 2$.

For a general displaced and anisotropic Gaussian, the angular coefficients can be obtained, as a function of r, through a direct angular integration. Otherwise, the power series for an exponential may be employed, in combination with the properties of spherical harmonics, to yield converging series for the coefficients. Specifically, as the argument of a source Gaussian is quadratic in coordinates, that argument can be represented in terms of harmonics of rank $\ell \leqslant 2$, leading to

$$\mathcal{S}(\boldsymbol{r}) = c(r) e^{\Gamma(\boldsymbol{r})}, \tag{78}$$

where

$$\begin{aligned}
\Gamma(\boldsymbol{r}) &= \sqrt{4\pi} \sum_{\substack{1 \leqslant \ell \leqslant 2 \\ m}} \Gamma^*_{\ell m}(r) Y_{\ell m}(\Omega) \\
&= \sum_{\substack{\vec{\ell} \\ 1 \leqslant \ell \leqslant 2}} \gamma(\vec{\ell}) \Gamma_{\vec{\ell}}(r) \hat{n}^{\ell_x} \hat{n}^{\ell_y} \hat{n}^{\ell_z}.
\end{aligned} \tag{79}$$

The exponential e^Γ may be next expanded in the power series, yielding

$$\mathcal{S}(\boldsymbol{r}) = \sum_{N=0}^{\infty} \mathcal{S}_N(\boldsymbol{r}), \tag{80}$$

where

$$\mathcal{S}_N(\boldsymbol{r}) = \mathcal{S}_{N-1}(\boldsymbol{r}) \frac{\Gamma(\boldsymbol{r})}{N}, \tag{81}$$

and $\mathcal{S}_0(r) = c(r)$. Individual terms of the sum in Eq. (80) may be represented in terms of the surface spherical harmonics of either type, leading to the corresponding expansion for the source $\mathcal{S}$. The rules of superposition for tesseral harmonics yield the following recursion relation for the tesseral expansion coefficients:

$$\begin{aligned}
\mathcal{S}_{N\ell m}(r) &= \frac{\sqrt{4\pi}}{N} \sum_{\ell' \ell'' m'} (\ell' m' \ell'' (m-m') | \ell m) \Gamma_{\ell' m'}(r) \\
&\quad \times \mathcal{S}_{(N-1)\ell''(m-m')}(r),
\end{aligned} \tag{82}$$

where $(\cdot|\cdot)$ represents a Clebsch-Gordan coefficient. It follows that terms in the sum (80) decrease rapidly with N, for $N \gg \max_{\ell m} |\Gamma_{\ell m}(r)|$. When aiming at the source in terms of Cartesian harmonic coefficients, first the Cartesian coefficients $\bar{\mathcal{S}}_{N\vec{\ell}}$ which do not meet the tracelessness condition are found through recursion:

$$\bar{\mathcal{S}}_{N\vec{\ell}}(r) = \frac{1}{N\gamma(\vec{\ell})} \sum_{\vec{m}} \gamma(\vec{m}) \gamma(\vec{\ell} - \vec{m}) \Gamma_{\vec{m}}(r) \bar{\mathcal{S}}_{(N-1)(\vec{\ell}-\vec{m})}(r). \tag{83}$$

In the next stage, the traceless coefficients $\mathcal{S}_{N\vec{\ell}}$ are found following such a procedure as in Eqs. (65)–(66). Finally, the

coefficients for the source may be obtained by summing over the respective series:

$$\mathcal{S}_{\ell m}(r) = \sum_{N=0}^{\infty} \mathcal{S}_{N\ell m}(r), \quad \text{or} \quad \mathcal{S}_{\bar{\ell}}(r) = \sum_{N=0}^{\infty} \mathcal{S}_{N\bar{\ell}}(r), \quad (84)$$

depending on whether the tesseral or Cartesian harmonics are followed. Coefficients for Gaussian sources in this section have been obtained following the recursion outlined above. Kernels for use in Eqs. (4) and (10) have been obtained using [29] known phase shifts.

To illustrate the possibility of measuring source shapes, we consider a relative source represented by an axially symmetric Gaussian oriented along the beam axis with parameters $R_x = R_y \equiv R_\perp = 4$ fm and $R_z = 8$ fm. For distinguishable particles, we additionally displace this Gaussian away from the origin at $r = 0$ by $\boldsymbol{d} = (0, 0, 4)$ fm. Such a source may result in consequence of emission of the individual species within two single-particle sources differently elongated along the z axis, with the source for the a species displaced by d along the z axis relative to the source for the b species. For the chosen relative source, the anisotropies of associated correlation functions can be quite significant. Examples of the associated correlations, for different particle pairs, pK^+, $p\pi^+$, pp, pn, nn, and $p\Lambda$, are presented in Fig. 5 as a function of $\cos\theta_{\boldsymbol{q}}$ at fixed q. The observed angular dependence of the functions is exclusively

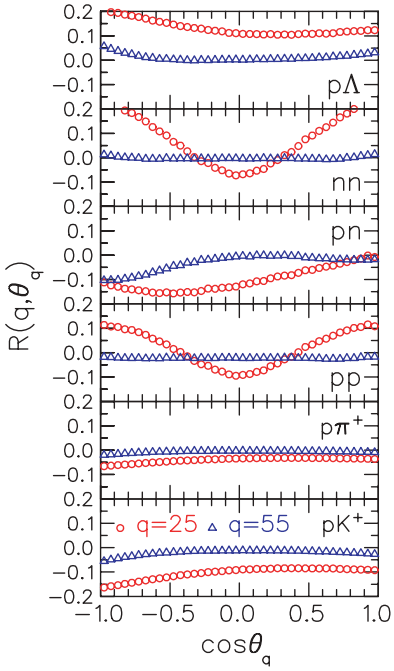

FIG. 5. (Color online) Correlations associated with a relative source in the form of an axially symmetric Gaussian, characterized by $R_x = R_y = 4$ fm and $R_z = 8$ fm, for different indicated particle pairs. For distinguishable particle pairs, the center of this Gaussian is shifted by $\boldsymbol{d} = (0, 0, 4)$ fm relative to the origin at $r = 0$. The correlations are shown as a function of cosine of the angle that the relative momentum $\boldsymbol{q}$ makes with the z axis, for two values of momentum magnitude $q = 25$ and 55 MeV/c. For the specific employed source, angular anisotropies in the correlation functions are of the same order as the functions.

due to the source anisotropy. While the correlations are stronger at low than at high q, the correlations and their anisotropies are generally of the same order. In the dependence of correlations on $\cos\theta_{\boldsymbol{q}}$, for distinguishable particles, one recognizes both odd and even components in $\cos\theta_{\boldsymbol{q}}$. The odd components are associated with the displacement $\boldsymbol{d}$ in the source, while the even are associated with both the displacement $\boldsymbol{d}$ and $R_\perp \neq R_z$. In the correlations of identical particles, only the effects of $R_\perp \neq R_z$ are present.

With the choice of axial symmetry for the specific source, all Cartesian components with odd number or x or y indices vanish. For identical particles, this further implies vanishing of Cartesian components with odd number of z indices, since there are no indices left to pair them with to yield a net even index number. For distinguishable particles at $\ell \leqslant 3$, the only nonvanishing moments are $\mathcal{S}^{(0)}$, $\mathcal{S}^{(1)}_z$, $\mathcal{S}^{(2)}_{xx}$, $\mathcal{S}^{(2)}_{yy}$, $\mathcal{S}^{(2)}_{zz}$, $\mathcal{S}^{(3)}_{xxz}$, $\mathcal{S}^{(3)}_{yyz}$, and $\mathcal{S}^{(3)}_{zzz}$. Not all of those moments are independent, as $\mathcal{S}^{(2)}_{xx} = -(\mathcal{S}^{(2)}_{yy} + \mathcal{S}^{(2)}_{zz})$ and $\mathcal{S}^{(3)}_{xxz} = -(\mathcal{S}^{(3)}_{yyz} + \mathcal{S}^{(3)}_{zzz})$, in consequence of the tensor tracelessness. In addition, the axial symmetry implies equality between components: $\mathcal{S}^{(2)}_{xx} = \mathcal{S}^{(2)}_{yy}$ and $\mathcal{S}^{(3)}_{xxz} = \mathcal{S}^{(3)}_{yyz}$. The left panels of Fig. 6 show the $\ell \leqslant 3$ Cartesian coefficients of correlations for proton-charged meson pairs. Those coefficients which

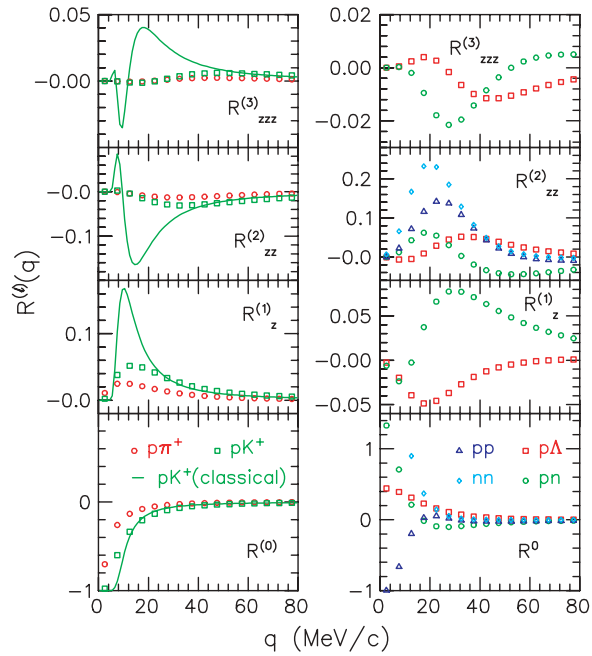

FIG. 6. (Color online) Angular coefficients of the correlations associated with an axially symmetric Gaussian source characterized by $R_x = R_y = 4$ fm and $R_z = 8$ fm, for proton-charged meson pairs (symbols in the left panels) and baryon-baryon pairs (symbols in the right panels), as a function of relative momentum q. For distinguishable particle pairs, the center of the Gaussian source is shifted by $\boldsymbol{d} = (0, 0, 4)$ fm relative to the origin at $r = 0$. The pK^+ and $p\pi^+$ correlations in the left panels tend to be dominated by the Coulomb interaction. To illustrate the degree to which quantal effects wash out the information on emission source, the left panels show also (solid lines) the pK^+ correlations in the limit of classical Coulomb interactions.

are not shown are easily generated from those shown, e.g., $\mathcal{S}^{(2)}_{xx} = -\mathcal{S}^{(2)}_{zz}/2$, etc.

The correlations of protons with charged mesons in Fig. 6 are plotted for $q < 80$ MeV/c. Within that momentum range, the correlation should be dominated by Coulomb effects. For comparison purposes, also shown in the figure are the pK^+ correlations expected in the classical limit of the Coulomb interactions. As expected following the discussions in Sec. II, the quantum effects seriously affect the correlations at $qR \lesssim \ell + \frac{1}{2}$, dampening out in that region the classical structures and hampering thus practical extraction of source shape information. With a smaller reduced mass in the $p\pi^+$ than in the pK^+ system, the classical Coulomb hole has a smaller q size in the $p\pi^+$ system. In consequence, the quantal effects have a stronger impact on the features of the $p\pi^+$ correlations, making the extraction of source shape harder from the $p\pi^+$ than from the pK^+ correlations.

Although difficult, it is certainly tenable to measure correlations of the order of 1% or less. To exhibit better the correlations at large q, Fig. 7 displays the same proton-charged meson correlations as those shown in Fig. 6, but they are now weighted by q^2. It is apparent that the correlations decrease as ℓ increases. An important feature of the exhibited correlations is that they are smooth in q for all ℓ. Because of this smooth behavior, it is possible to analyze those correlations utilizing wide momentum bins. The phase space increasing as q^2 should further help one to garner statistics needed for analyzing the correlations at the level of 1% or less. The practical limitation for the analysis at large q, though, may turn out to be the need to separate the correlations due to final-state effects within the pair from the possible competing correlations induced by collective flow and, at RHIC, by jets.

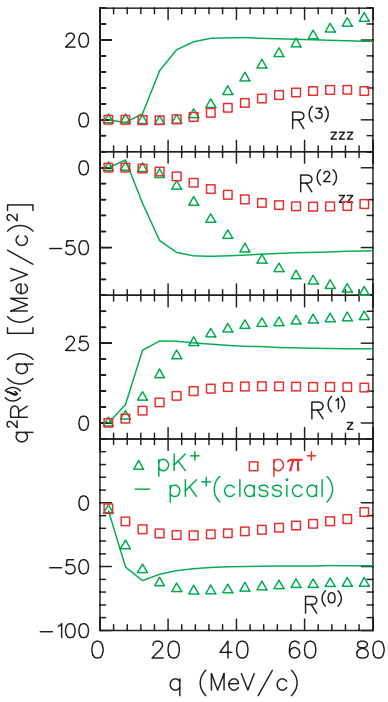

FIG. 7. (Color online) Same proton-charged meson correlation coefficients as in Fig. 6, but now multiplied by the factor of q^2 to better exhibit the features of the correlations at large q.

Correlations of elementary baryons are good candidates for source analyses because of the large scattering lengths within the pairs which lead to strong correlation structures on the relative-momentum scale of $q \sim 20$ MeV/c. The right-side panels of Fig. 6 display the correlations for pn, nn, pp, and $p\Lambda$ pairs, associated with the Gaussian sources. When present, the $\ell \geqslant 1$ baryon-baryon correlations tend to be significantly stronger at most momenta of experimental interest than the corresponding Coulomb-dominated meson-baryon correlations. The odd correlation moments vanish for the pp and nn pairs as the pair sources and correlations are symmetric under particle interchange. The odd-ℓ correlations are especially important for the pn pairs emitted from intermediate-energy heavy ion collisions, because these correlations tie to the issue of whether neutrons are emitted earlier than protons and, further, to the symmetry energy. Within high-energy collisions, odd-ℓ $p\Lambda$ correlations are of interest as they can provide information on whether the hyperons leave earlier than protons.

B. Boost-invariant blast-wave sources

Results of early pion-pion correlation measurements at RHIC have been satisfactorily described with fits within the blast-wave models [37,38]. Those fits have suggested a nearly instantaneous emission, directly contradicting the formation of a long-lived mixed phase which would have resulted in a dilatory emission and in relative sources with sizes extended in the outward direction of the pair total momentum. Given the importance of those measurements and findings, it is important to verify the conclusions on the nature of particle emission at RHIC by extracting sources from the correlations of other pairs such as involving kaons or protons. The minimal blast-wave model used here for illustration employs four parameters describing the single-particle sources that are boost invariant along the beam axis:

$$s(\boldsymbol{p}, \boldsymbol{r}, t) \times \propto \delta(\tau - \tau_f)\theta(r_{\max} - r_\perp) m_\perp \cosh(y - \eta) \exp\left(-\frac{p^\mu u_\mu}{T}\right). \tag{85}$$

Here, y and η are, respectively, energy-momentum and space-time longitudinal rapidities. The emission is assumed to occur at one proper time $\tau_f = 10$ fm/c. The decoupling is assumed to be spread out over the cylindrical volume of radius $r_{\max} = 13$ fm and to take place in the presence of a collective motion characterized by transverse rapidity ρ ($u_\perp = \sin\rho$) proportional to transverse position, $\rho \propto r_\perp$, producing the maximal transverse velocity in the longitudinal center of mass of $v_\perp^{\max} = \tanh\rho^{\max} = 0.75c$, at $r_\perp = r_{\max}$. The breakup temperature is assumed to be $T = 105$ MeV/c. The chosen parameters describe [37] particle spectra at $p_\perp < 1$ GeV/c, as well as basic aspects of pion-pion correlations, in Au+Au collisions at $\sqrt{s_{NN}} = 130$ GeV. Here, our goal is not to fit data but to use the blast-wave model to see what results might be expected for correlations of other particle pairs analyzed in terms of $\mathcal{R}^{(\ell)}(q)$.

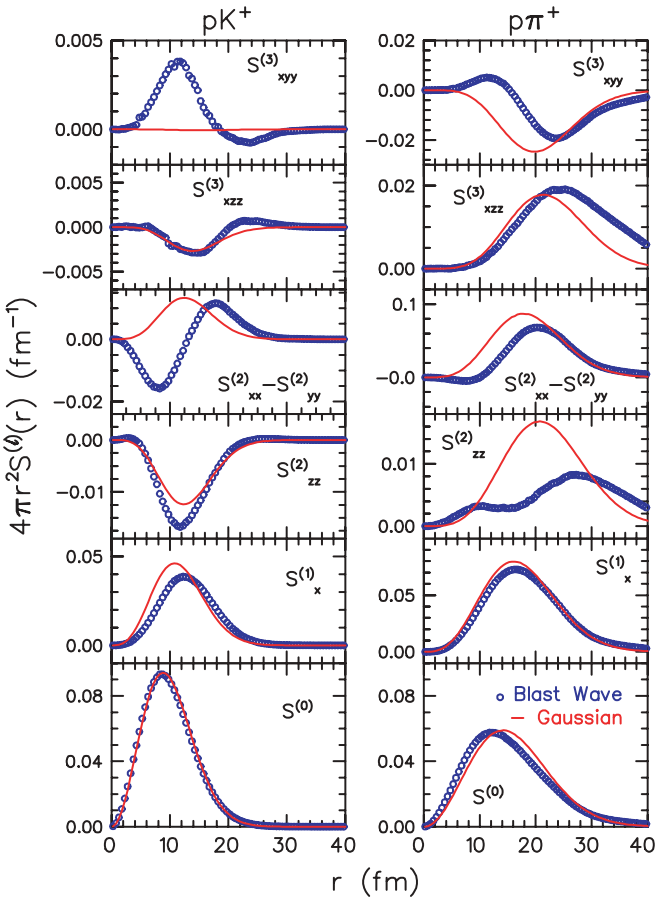

FIG. 8. (Color online) Angular Cartesian coefficients at $\ell \leqslant 3$, multiplied by $4\pi r^2$, of relative sources for pK^+ (left) and $p\pi^+$ (right) pairs moving out at transverse velocity of $0.6c$ relative to the beam axis. Symbols represent the results obtained in the blast-wave model. Lines represent the results from a Gaussian source with the same pair c.m. Cartesian moments, $\langle r_i \rangle$ and $\langle r_i r_j \rangle$, as the blast-wave source. The non-Gaussian features of a blast-wave source become more apparent as the mass difference within a pair increases.

We focus on correlations of nonidentical particles because of the possibility for associated finite odd angular moments. The $\ell \leqslant 3$ relative-source moments for the pK and $p\pi$ pairs moving at transverse velocity of $v_\perp = 0.6c$ are shown in Fig. 8. To obtain the displayed results, emission positions $\boldsymbol{r}_{a,b}$ for each of the particles a and b were generated within the particle rest frame following the blast-wave description. After several thousand points were generated, the number of relative positions $\boldsymbol{r}_a - \boldsymbol{r}_b$ for the relative source became of the order of a few million, sufficient for finding quite smooth source moments, except at the lowest $|\boldsymbol{r}_a - \boldsymbol{r}_b|$. We associate the z-axis direction with the beam axis and the x-axis direction with the outward direction along the pair momentum. The angular moments for the blast-wave model are compared in Fig. 8 to the moments for a Gaussian source with the same Cartesian moments, $\langle x \rangle$, $\langle x^2 \rangle$, $\langle y^2 \rangle$, and $\langle z^2 \rangle$, as the blast-wave relative source.

As elsewhere, values for the underlying three-dimensional source structure can be restored along any direction from the Cartesian coefficients, in particular from those displayed in Fig. 8, exploiting tracelessness. Thus, e.g., along the x axis the source values are

$$\mathcal{S} = \mathcal{S}^{(0)} \pm \mathcal{S}^{(1)}_x + \tfrac{1}{2}\left(S^{(2)}_{xx} - S^{(2)}_{yy}\right) - \tfrac{1}{2}S^{(2)}_{zz} \mp S^{(3)}_{xyy} \mp S^{(3)}_{xzz} + \ldots, \tag{86}$$

where the upper and lower signs refer to the positive and negative directions along the axis. Within the xy plane, at 45° to the x axis, the source values are

$$\mathcal{S} = \mathcal{S}^{(0)} \pm \frac{1}{\sqrt{2}}\mathcal{S}^{(1)}_x - \frac{1}{2}S^{(2)}_{zz} \mp \frac{1}{2\sqrt{2}}S^{(3)}_{xzz} + \cdots, \tag{87}$$

with the upper signs again referring to the positive direction along the x axis.

Within the blast-wave model, the heavier particles end up being emitted farther out, on the average, along the outward direction, than the lighter particles. This is due to the following. In an infinite system with Hubble expansion, a particle with a given velocity would be, on the average, emitted from a spatial patch centered around the point with the collective velocity matching the particle velocity. The size of such an emission patch would depend on the particle mass, with the patch being tighter for heavier particles with lower thermal velocities and being more extended for lighter particles. Relative to the infinite system, however, in a system with a finite transverse extension, the outer portions of the emission patches would get cut off and more so for the light than for heavy particles, forcing the emission region of the light particles inward relative to the heavy ones. In the past, relative displacements of emission between particles of different mass, e.g., $K\pi$, have been accessed by comparing the correlations at opposite signs of outward momentum, $q_{\rm out} > 0$ and $q_{\rm out} < 0$, at low values of the remaining q components [39,40]. Such a strategy discards potentially useful information on the relative displacement in the remainder of the relative momentum space. The displacement of species within a pair is visible in Fig. 8 in the finite values of $\mathcal{S}^{(1)}_x$. With the mass difference being larger within the $p\pi$ than the pK pairs, the $\mathcal{S}^{(1)}_x$ coefficients peak farther out and reach significantly higher values for the $p\pi$ than the pK pairs.

Some other features of blast-wave sources become apparent in the context of comparisons with Gaussian sources. When making such a comparison, a few points need to be kept in mind. In an infinite system with a Hubble-like expansion along the longitudinal direction, the associated relative source should fall off exponentially at large r in the longitudinal direction, rather than falling in a Gaussian fashion; see, e.g., Eq. (74). On the other hand, when the emission within a model is confined to a finite transverse domain, the source function should fall off more sharply in the transverse directions, especially in the sideward direction which is less affected by decays. For our comparison, we chose the parameters of the Gaussian source to match the norm and $\langle r_i \rangle$ and $\langle r_i r_j \rangle$ of the blast-wave source. Given Eq. (53), this means that the $\ell \leqslant 2$ integrals of $r^{\ell+2}\mathcal{S}^{(\ell)}(r)$ for the Gaussian are made to match those for the blast wave.

When comparing the blast-wave and Gaussian source coefficients in Fig. 8, we can see that the agreement between

them generally worsens as ℓ increases, and it is worse for $p\pi$ than for pK pairs. These tendencies are to an extent associated with the source tails. Since the emission region is wider in the case of pions than kaons, the larger-scale geometry of the emitting region is explored more stringently in the case of pions. In addition, the pions become relativistic at lower p_t than do kaons. The finite transverse extension of the emission zone most strongly suppresses the tail of the relative source in the negative x direction. In terms of angular coefficients, this suppression generally results in a large enhancement of the high-ℓ blast-wave coefficients at high r, compared with the Gaussian coefficients. This enhancement is particularly visible for the $p\pi$ pairs. The one case in Fig. 8 where the $p\pi$ $\mathcal{S}^{(2)}_{zz}$ is smaller in magnitude for the blast-wave than the Gaussian source is associated with the change in sign for that coefficient. The change in sign is itself associated with the trimming of the relative source by extension of the emitting region, present in the x and y directions, but absent in the z direction. Further sign changes are seen for the blast-wave $\ell = 3$ coefficients, while there are no such changes for the corresponding Gaussian coefficients. These sign changes reflect the more complex nature of the blast-wave sources of a crescent-like shape in the xy and xz directions. The latter shape results from the relativistically noninstantaneous nature of the boost-invariant blast-wave emission, mentioned already in the preceding section. Coded in the $\mathcal{S}^{(3)}_{xyy}$ and $\mathcal{S}^{(3)}_{xzz}$ coefficients, cf. Eq. (53), are the violations of the factorizations which hold for the Gaussian source: $\langle xy^2\rangle = \langle x\rangle\langle y^2\rangle$ and $\langle xz^2\rangle = \langle x\rangle\langle z^2\rangle$. These violations result in significant differences between the $\ell = 3$ coefficients for the Gaussian and blast wave.

Regarding the examples of source coefficients in Fig. 8, it is important to note that while the $\ell = 0$ coefficients have most of their strength within the 5–15 fm region of separation, the $\ell \geqslant 1$ coefficients have most of their strength within the 7–25 fm region. The fact that the source anisotropies are most pronounced at large r, combined with the difference in falloff for strong and Coulomb kernels of $1/r^2$ vs $1/r$, allows the Coulomb-induced correlations to compete effectively with the correlations induced by strong interactions in providing access to the source anisotropies.

Figure 9 displays the proton-charged meson correlations calculated by convoluting the source functions illustrated in Fig. 8 with the respective kernels. The utilized pK^+ and $p\pi^+$ kernels have been obtained accounting both for the Coulomb as well as the strong interactions [29]. Relative magnitudes of discrepancies between the blast wave and Gaussian are similar for the corresponding correlation and source coefficients. The level of difficulty in accessing the shape information may be assessed in Fig. 9 by examining the absolute magnitudes of coefficients for the different ℓ values. For $\ell = 1$, the magnitude is of the order of a few percent, which should be observable with statistics characteristic for the past correlation measurements. For $\ell \geqslant 2$, the magnitude is of the order of 1% and less. Particularly well suited for investigating the high-ℓ correlations should be the high-statistics data from the 2004 run at RHIC. Eventually, the reach of the analysis may be limited by systematics rather than by statistics.

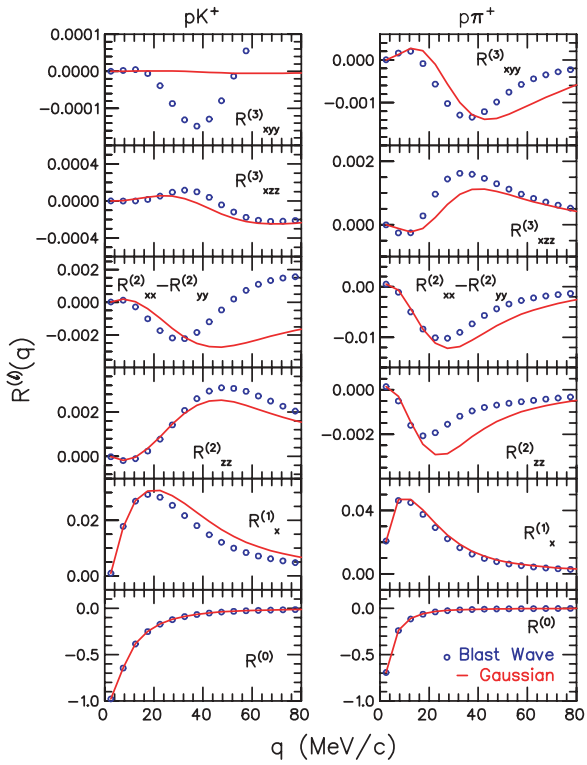

FIG. 9. (Color online) Cartesian coefficients for the correlations of pK^+ (left) and $p\pi^+$ (right) pairs moving out at transverse velocity of $0.6c$ relative to the beam axis. Symbols represent the results obtained in the blast-wave model, while lines represent the results from a Gaussian source with the same pair c.m. Cartesian moments, $\langle r_i\rangle$ and $\langle r_i r_j\rangle$, as the blast-wave source. The corresponding Cartesian source coefficients have been represented in Fig. 8. As in Fig. 8, differences between the blast-wave and Gaussian results are more pronounced for the $p\pi^+$ than for pK^+ pairs.

VI. SUMMARY

Correlation measurements are a crucial tool for understanding the dynamics of central nuclear reactions. One of the forefront tasks of a correlation analysis is to decipher the mire of RHIC data. Without carrying out a multidimensional correlation analysis, there is little chance for a detailed understanding of the impact of dynamics on correlations in those reactions or for understanding the role played by the equation of state. To date, correlation analyses at RHIC have focused on identical pions. In identical-pion correlations, strong interactions play little role. In the analyses to date, Coulomb interactions have been normally corrected for in a shape-independent manner, leaving off correlations induced by identical-particle interference. The latter are related to the source through Fourier transformation allowing for easy modeling with specific sources such as Gaussian. The decomposition of correlations in terms of Cartesian coefficients offers an alternative way of carrying out a multidimensional correlation analysis for identical pion pairs and it provides the possibility for carrying out multidimensional analysis for other classes of final-state effects.

One of the benefits of decomposing information with angular harmonics is that the correlations induced by Coulomb

and strong interactions carry, on their own, some shape information that can be exploited in the correlation analysis. The representation of the correlations in terms of the Cartesian or tesseral coefficients carries the full three-dimensional information in terms of a set of one-dimensional functions. Data represented in this fashion can be then be compared with models visually, one harmonic at a time, providing the means to better identify which shape characteristics of the data are being described by the model.

The ability to discern information about source shapes from correlation measurements depends on the structure of the kernels, $\mathcal{K}_\ell(q,r)$, for different spherical ranks ℓ. In Sec. II, we demonstrated that the identical-particle interference, Coulomb interactions, and strong interactions all produce effective kernels. The resolving power of Coulomb interactions was shown to rise with mass and charge within the interacting pair. Strong interactions are most effective in the resonance region and, otherwise, for large cross sections. Even purely s-wave interactions can produce kernels of good resolving power at higher ℓ.

While expansions employing tesseral harmonics nominally provide means that are as powerful for storing information in correlation functions as those employing Cartesian harmonics, the basis is not as transparent or as intuitive. Cartesian harmonics have a variety of useful properties which can be exploited in manipulating the angular information, as was shown in Sec. III. The connection between specific aspects of the source geometry and specific angular moments has been emphasized in Sec. IV. It has been pointed out that the average relative displacement of emission points in the c.m. frame of nonidentical particles can be assessed through the $\ell = 1$ angular moments. The quadrupole distortion, most commonly quantified in terms of the radii $R_{\rm out}$, $R_{\rm side}$, and $R_{\rm long}$, can be studied with the $\ell = 2$ moments. The $\ell = 3$ moments test the more complex aspects of sources such as boomerang features.

Detailed examples of sources and correlations have been presented in Sec. V. Using Gaussian sources, it has been, in particular, demonstrated that the pK^+ and $p\pi^+$ correlations can realistically be expected to provide shape information on emission sources. The strengths of correlations characterizing shape anisotropies can reach the magnitude of a few percent. While the upcoming RHIC data sets will provide sufficient statistics to assess correlations between different particles at the level of 1% or better, the true challenge may turn out to be the subtraction of competing correlations, such as those produced by jets. The proton-charged meson correlations are dominated by Coulomb interactions. The strong interactions in baryon-baryon systems, though, can also provide good means for discerning shape anisotropies at low relative momenta, yielding correlations of the same order or larger than the proton-meson correlations. One common feature of all pairs and sources examined here is that the variation of the correlation with angle is comparable in magnitude to the angle-integrated correlation. Consequently, if one has sufficient statistics to measure a one-dimensional correlation, only a modest enhancement in statistics would suffice to find, or constrain in a meaningful manner, the higher angular moments. In the context of the blast-wave sources, opportunities for detecting more complex shapes have been discussed, such as boomerang shapes.

In conclusion, a treasure trove of potential information lies largely ignored in the huge volumes of data from high-energy collisions. This information can address what is the perhaps the greatest surprise of the first several years of RHIC experiments, the source sizes and shapes inferred from identical-pion correlations. The main difficulty with the proposed new class of correlation analyses is that they rely on observables that are quantitatively small, of the order of a percent. This will require a careful analysis of competing correlations from jets and collective flow, but we believe that the objectives will indeed prove feasible.

ACKNOWLEDGMENTS

The authors acknowledge insightful discussions with Paul Chung, David Brown, and Richard Lednicky. Support was provided by the U.S. National Science Foundation, Grant No. PHY-0555893, and by the U.S. Department of Energy, Grant No. DE-FG02-03ER41259.

APPENDIX: PROJECTION OPERATOR $\mathcal{P}$

In arriving at the Cartesian harmonics, an important role has been played by the Cartesian projection operator $\mathcal{P}$ which projects out the symmetric traceless portion of any Cartesian tensor. As a projection operator, $\mathcal{P}$ must have the following properties:

$$\mathcal{P}^{(\ell:\ell)}_{\alpha_1\ldots\alpha_\ell:\alpha'_1\ldots\alpha'_\ell} = \mathcal{P}^{(\ell:\ell)}_{\alpha'_1\ldots\alpha'_\ell:\alpha_1\ldots\alpha_\ell}, \tag{A1}$$

$$\mathcal{P}^{(\ell:\ell)}_{\alpha_1\ldots\alpha_\ell:\alpha'_1\ldots\alpha'_\ell} = \sum_{\alpha''_1\ldots\alpha''_\ell} \mathcal{P}^{(\ell:\ell)}_{\alpha_1\ldots\alpha_\ell:\alpha''_1\ldots\alpha''_\ell} \mathcal{P}^{(\ell:\ell)}_{\alpha''_1\ldots\alpha''_\ell:\alpha'_1\ldots\alpha'_\ell}. \tag{A2}$$

The projection operator acting on any tensor T must yield a traceless result $\mathcal{P}T$. Since we can choose, in particular, a tensor that is finite for any single set of indices and zero otherwise, we find that the operator $\mathcal{P}$ itself must be traceless:

$$\sum_\alpha \mathcal{P}^{(\ell:\ell)}_{\alpha_1\ldots\alpha_{\ell-2}\alpha\alpha:\alpha'_1\ldots\alpha'_\ell} = \sum_\alpha \mathcal{P}^{(\ell:\ell)}_{\alpha_1\ldots\alpha_\ell:\alpha'_1\ldots\alpha'_{\ell-2}\alpha\alpha} = 0. \tag{A3}$$

We shall demonstrate existence of the operator $\mathcal{P}$ by construction. Notably, when acting onto a symmetrized traceless tensor, the operator must reproduce the tensor. Thus, we can represent $\mathcal{P}$ as

$$\mathcal{P}^{(\ell:\ell)}_{\alpha_1\ldots\alpha_\ell:\alpha'_1\ldots\alpha'_\ell} = S^{(\ell:\ell)}_{\alpha_1\ldots\alpha_\ell:\alpha'_1\ldots\alpha'_\ell} + \Delta\mathcal{P}^{(\ell:\ell)}_{\alpha_1\ldots\alpha_\ell:\alpha'_1\ldots\alpha'_\ell}, \tag{A4}$$

or, in shortened notation,

$$\mathcal{P}^{(\ell:\ell)} = S^{(\ell:\ell)} + \Delta\mathcal{P}^{(\ell:\ell)}, \tag{A5}$$

where S is the symmetrized identity operator

$$S^{(\ell:\ell)}_{\alpha_1\ldots\alpha_\ell:\alpha'_1\ldots\alpha'_\ell} = \frac{1}{\ell!}\sum_{\sigma\in\Pi(\ell)} \delta_{\alpha_{\sigma(1)}\alpha'_1}\ldots\delta_{\alpha_{\sigma(\ell)}\alpha'_\ell}, \tag{A6}$$

and $\Delta\mathcal{P}$ is an operator which yields a zero when acting upon a traceless tensor. In Eq. (A6), the sum is over permutations of ℓ indices. Importantly, a traceless symmetric tensor of rank

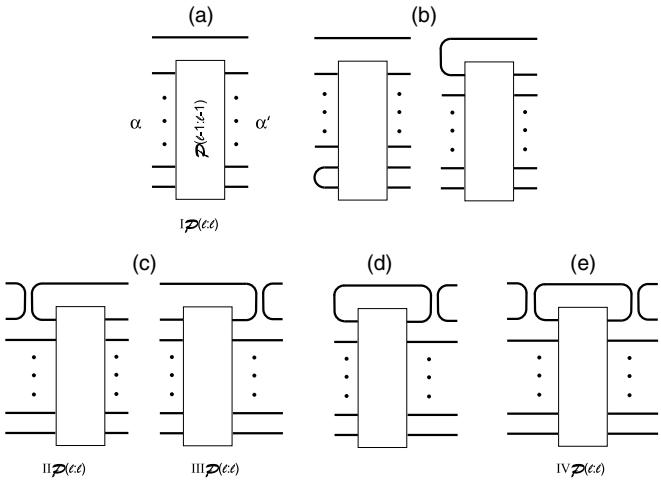

FIG. 10. Diagrams illustrating the construction of the projection operator $\mathcal{P}^{(\ell:\ell)}$, using the lower-rank operator $\mathcal{P}^{(\ell-1:\ell-1)}$, represented by the rectangular block, and δ symbols, represented by lines. (a) Leading term ${}^{\mathrm{I}}\mathcal{P}^{(\ell:\ell)}$, Eq. (A8). (b) Terms resulting from evaluating the trace of ${}^{\mathrm{I}}\mathcal{P}^{(\ell:\ell)}$; terms in left diagram yield zero due to the tracelessness of $\mathcal{P}^{(\ell-1:\ell-1)}$. (c) ${}^{\mathrm{II}}\mathcal{P}^{(\ell:\ell)}$ and ${}^{\mathrm{III}}\mathcal{P}^{(\ell:\ell)}$ terms within the construct of Eqs. (A9) and (A10), respectively. (d) Nonvanishing terms from evaluating the trace of ${}^{\mathrm{III}}\mathcal{P}$. (e) Final ${}^{\mathrm{IV}}\mathcal{P}^{(\ell:\ell)}$ term within the construct Eq. (A11).

ℓ' is traceless and symmetric within any subset $\ell < \ell'$ of its indices. When acting on any of ℓ indices of a rank-ℓ', $\ell' > \ell$, traceless tensor, the constructed operator $\mathcal{P}^{(\ell:\ell)}$ will reproduce that tensor and $\Delta\mathcal{P}^{(\ell:\ell)}$ alone will annihilate it.

In our construction of $\mathcal{P}$, we will find useful a graphical method similar to that employed for interactions [41]. Within the method, the Kronecker $\delta_{\alpha\alpha'}$ is represented as a line joining the indices α and α'. A convolution of δ symbols $\sum_{\alpha_1\ldots\alpha_n} \delta_{\alpha\alpha_1}\delta_{\alpha_1\alpha_2}\ldots\delta_{\alpha_n\alpha'} = \delta_{\alpha\alpha'}$ is represented by joining the line segments, which produces a single line from α to α'. A line which closes on itself represents a scalar factor which is the trace of the δ symbol, equal to the dimension of space, $\sum_\alpha \delta_{\alpha\alpha} = 3$. Examples are provided in Fig. 10.

For $\ell = 0$ and $\ell = 1$, the operator $\mathcal{P}$ is simply the identity operator, $\mathcal{P}^{(0:0)} = 1$ and $\mathcal{P}^{(1:1)}_{\alpha:\alpha'} = \delta_{\alpha\alpha'}$. We will show that when the operator for the rank $(\ell-1)$ tensors is known, it is possible to construct the operator with the required properties for the next rank-ℓ tensors. Thus, the operator for any rank can be constructed by recursion. Let us assume that we know the operator for rank $(\ell-1)$, $\mathcal{P}^{(\ell-1:\ell-1)}$. We shall construct the next rank operator as a sum of terms,

$$\mathcal{P}^{(\ell;\ell)} = {}^{\mathrm{I}}\mathcal{P}^{(\ell;\ell)} + {}^{\mathrm{II}}\mathcal{P}^{(\ell;\ell)} + \cdots, \tag{A7}$$

exploiting the operator $\mathcal{P}^{(\ell-1:\ell-1)}$. The terms of different structure will be added to achieve in Eq. (A7) the properties in Eqs. (A1)–(A3) for $\mathcal{P}^{(\ell:\ell)}$. In particular, only ${}^{\mathrm{I}}\mathcal{P}$ in our construction will contain the symmetrization operator S on the right-hand side of Eq. (A5).

Since, within each rank, the operator must not only contain a symmetrized identity operator but also be traceless, it is natural to start with ${}^{\mathrm{I}}\mathcal{P}$ as a tensor product of the lower-rank operator and identity, illustrated in Fig. 10(a),

$$\delta_{\alpha_\ell\alpha'_\ell}\mathcal{P}^{(\ell-1;\ell-1)}_{\alpha_1\ldots\alpha_{\ell-1}:\alpha'_1\ldots\alpha'_{\ell-1}}, \tag{A8}$$

symmetrized separately in the index sets α and α'. Evaluation of the trace for ${}^{\mathrm{I}}\mathcal{P}$ produces terms which correspond to the trace of the lower-rank operator $\mathcal{P}^{(\ell-1:\ell-1)}$, represented by the left diagram in Fig. 10(b), and to the convolutions of the δ symbol with $\mathcal{P}^{(\ell-1:\ell-1)}$, represented by right diagram in Fig. 10(b). Terms of the first type yield zero due to the tracelessness of $\mathcal{P}^{(\ell-1:\ell-1)}$, but those of the second type generally yield a finite contribution. Aiming at the tracelessness of $\mathcal{P}^{(\ell:\ell)}$, one can next add to the construct a counter-term ${}^{\mathrm{II}}\mathcal{P}$ of the form

$$-c_{\mathrm{II}}\delta_{\alpha_{\ell-1}\alpha_\ell}\mathcal{P}^{(\ell-1;\ell-1)}_{\alpha_1\ldots\alpha_{\ell-2}\alpha'_\ell:\alpha'_1\ldots\alpha'_{\ell-1}}, \tag{A9}$$

to cancel the last contribution, symmetrized separately in the indices α and α', represented by the left diagram in Fig. 10(c). The constant c_{II} should be adjusted to achieve the tracelessness of $\mathcal{P}^{(\ell:\ell)}$. Taking the trace of ${}^{\mathrm{II}}\mathcal{P}$ produces the same type of terms as for ${}^{\mathrm{II}}\mathcal{P}$, that were represented in Fig. 10(b). Thus, an adjustment of c_{II} can indeed produce a traceless sum ${}^{\mathrm{I}}\mathcal{P} + {}^{\mathrm{II}}\mathcal{P}$. However, the operator $\mathcal{P}^{(\ell:\ell)}$ should be symmetric under the transposition of the indices α and α', Eq. (A1). In consequence, when adding the term ${}^{\mathrm{II}}\mathcal{P}$ to the construction, one also needs to add a term ${}^{\mathrm{III}}\mathcal{P} = ({}^{\mathrm{II}}\mathcal{P})^\top$, of the form

$$-c_{\mathrm{II}}\delta_{\alpha'_{\ell-1}\alpha'_\ell}\mathcal{P}^{(\ell-1;\ell-1)}_{\alpha_1\ldots\alpha_{\ell-1}:\alpha'_1\ldots\alpha'_{\ell-2}\alpha_\ell}, \tag{A10}$$

symmetrized separately in the index sets α and α' and represented by the right diagram in Fig. 10(c). The nonvanishing terms from evaluating the trace of ${}^{\mathrm{III}}\mathcal{P}$ are illustrated in Fig. 10(d). That last contribution to the trace may be compensated for by adding the final term ${}^{\mathrm{IV}}\mathcal{P}$ to the construct, symmetric under transposition, of the form

$$c_{\mathrm{IV}}\delta_{\alpha_{\ell-1}\alpha_\ell}\delta_{\alpha'_{\ell-1}\alpha'_\ell}\sum_\beta \mathcal{P}^{(\ell-1;\ell-1)}_{\alpha_1\ldots\alpha_{\ell-2}\beta:\alpha'_1\ldots\alpha'_{\ell-2}\beta}, \tag{A11}$$

symmetrized separately in the indices α and α', and illustrated with the diagram in Fig. 10(d). Taking the trace of ${}^{\mathrm{IV}}\mathcal{P}$ produces, up to a factor, the same result as taking the trace of ${}^{\mathrm{III}}\mathcal{P}$.

The constants c_{II} and c_{IV} can be now set to make the trace of $\mathcal{P}^{(\ell;\ell)}$ vanish. The net result for the operator, with the symmetrizations made explicit, is

$$\mathcal{P}^{(\ell;\ell)}_{\alpha_1\ldots\alpha_\ell:\alpha'_1\ldots\alpha'_\ell} = \frac{1}{\ell^2}\sum_{m,n=1}^{\ell}\delta_{\alpha_m\alpha'_n}\mathcal{P}^{(\ell-1:\ell-1)}_{\alpha_1\ldots\alpha_{m-1}\alpha_{m+1}\ldots\alpha_\ell:\alpha'_1\ldots\alpha'_{n-1}\alpha'_{n+1}\ldots\alpha'_\ell}$$
$$-\frac{2}{\ell^2(2\ell-1)}\sum_{\substack{1\leqslant m<r\leqslant\ell\\ 1\leqslant n\leqslant\ell}}\delta_{\alpha_m\alpha_r}\mathcal{P}^{(\ell-1:\ell-1)}_{\alpha_1\ldots\alpha_{m-1}\alpha_{m+1}\ldots\alpha_{r-1}\alpha_{r+1}\ldots\alpha_\ell\alpha'_n:\alpha'_1\ldots\alpha'_{n-1}\alpha'_{n+1}\ldots\alpha'_\ell}$$

$$-\frac{2}{\ell^2(2\ell-1)}\sum_{\substack{1\leqslant m\leqslant \ell\\ 1\leqslant n<s\leqslant \ell}}\delta_{\alpha'_n\alpha'_s}\mathcal{P}^{(\ell-1:\ell-1)}_{\alpha_1\ldots\alpha_{m-1}\alpha_{m+1}\ldots\alpha_\ell:\alpha'_1\ldots\alpha'_{n-1}\alpha'_{n+1}\ldots\alpha'_{s-1}\alpha'_{s+1}\ldots\alpha'_\ell\alpha_m}$$

$$+\frac{4}{\ell^2(2\ell-1)^2}\sum_{\substack{1\leqslant m<r\leqslant \ell\\ 1\leqslant n<s\leqslant \ell}}\delta_{\alpha_m\alpha_r}\,\delta_{\alpha'_n\alpha'_s}\sum_{\beta}\mathcal{P}^{(\ell-1:\ell-1)}_{\alpha_1\ldots\alpha_{m-1}\alpha_{m+1}\ldots\alpha_{r-1}\alpha_{r+1}\ldots\alpha_\ell\beta:\alpha'_1\ldots\alpha'_{n-1}\alpha'_{n+1}\ldots\alpha'_{s-1}\alpha'_{s+1}\ldots\alpha'_\ell\beta}. \tag{A12}$$

By now, we have constructed an operator $\mathcal{P}^{(\ell;\ell)}$ which is symmetric separately in the covariant and contravariant indices, traceless, and symmetric under the transposition. The remaining question is whether repeated applications of the operator yield the same result, i.e., whether Eq. (A1) is satisfied.

To answer the last question, let us apply $\mathcal{P}^{(\ell;\ell)}$, out of the four components in Eqs. (A7) and (A12), to the constructed $\mathcal{P}^{(\ell;\ell)}$ with the properties we have established. The ${}^1\mathcal{P}$ component reproduces $\mathcal{P}^{(\ell;\ell)}$, as both the Kronecker symbol and $\mathcal{P}^{(\ell-1;\ell-1)}$ reproduce a traceless symmetric tensor. On the other hand, all the other components of the construct annihilate $\mathcal{P}^{(\ell;\ell)}$, because they involve calculation of the trace of that operator, either directly or after application of $\mathcal{P}^{(\ell-1;\ell-1)}$. Thus, Eq. (A1) is satisfied.

Use of Eq. (A12) for $\ell = 2$ produces

$$\mathcal{P}^{(2:2)}_{\alpha_1\alpha_2:\alpha'_1\alpha'_2}=\tfrac{1}{2}\left(\delta_{\alpha_1\alpha'_1}\delta_{\alpha_2\alpha'_2}+\delta_{\alpha_1\alpha'_2}\delta_{\alpha_2\alpha'_1}\right)-\tfrac{1}{3}\delta_{\alpha_1\alpha_2}\delta_{\alpha'_1\alpha'_2}. \tag{A13}$$

In general, for $\mathcal{P}^{(\ell;\ell)}$ at $\ell\geqslant 2$, the repeated recursion with Eq. (A12) produces, besides the leading symmetrized identity term, the correction terms which involve replacing k pairs of Kronecker symbols in the identity linking the covariant and contravariant indices, with the pairs of Kronecker symbols linking separately the covariant and contravariant indices, $k = 1, 2, \ldots, \ell/2$. Application of both sides of Eq. (A12) for $\mathcal{P}$ to $\boldsymbol{n}^\ell$ produces the recursion relation (49) for $\mathcal{A}$.

[1] U. W. Heinz and B. V. Jacak, Annu. Rev. Nucl. Part. Sci. **49**, 529 (1999).
[2] W. Bauer, C. K. Gelbke, and S. Pratt, Annu. Rev. Nucl. Part. Sci. **42**, 77 (1992).
[3] U. A. Wiedemann and U. W. Heinz, Phys. Rep. **319**, 145 (1999).
[4] B. Tomasik and U. A. Wiedemann, in *Quark-Gluon Plasma 3*, edited by R. C. Hwa and X.-N. Wang (World Scientific, Singapore, 2004).
[5] C. Adler *et al.* (STAR Collaboration), Phys. Rev. Lett. **87**, 082301 (2001).
[6] K. Adcox *et al.* (PHENIX Collaboration), Phys. Rev. Lett. **88**, 192302 (2002).
[7] M. Baker *et al.* (PHOBOS Collaboration), Nucl. Phys. **A715**, 65 (2003).
[8] M. Gyulassy and D. Rischke, Nucl. Phys. **A608**, 479 (1996).
[9] D. Teaney, J. Lauret, and E. Shuryak, nucl-th/0110037.
[10] S. Soff, S. Bass, and A. Dumitru, Phys. Rev. Lett. **86**, 3981 (2001).
[11] P. F. Kolb and U. Heinz (2003), in *Quark-Gluon Plasma 3*, edited by R. C. Hwa and X.-N. Wang (World Scientific, Singapore, 2004).
[12] J. Applequist, J. Phys. A **22**, 4303 (1989).
[13] D. Anchishkin, U. W. Heinz, and P. Renk, Phys. Rev. C **57**, 1428 (1998), nucl-th/9710051.
[14] P. Danielewicz and P. Schuck, Phys. Lett. **B274**, 268 (1992).
[15] S. Pratt, Phys. Rev. D **33**, 1314 (1986).
[16] G. F. Bertsch, Nucl. Phys. **A498**, 173c (1989).
[17] T. Csorgo, J. Zimanyi, J. Bondorf, H. Heiselberg, and S. Pratt, Phys. Lett. **B241**, 301 (1990).
[18] G. Verde, P. Danielewicz, D. A. Brown, W. G. Lynch, C. K. Gelbke, and M. B. Tsang, Phys. Rev. C **67**, 034606 (2003).
[19] G. Verde, P. Danielewicz, C. K. Gelbke, W. G. Lynch, and M. B. Tsang, Phys. Rev. C **65**, 054609 (2002).
[20] S. Y. Panitkin *et al.* (E895 Collaboration), Phys. Rev. Lett. **87**, 112304 (2001).
[21] D. A. Brown and P. Danielewicz, Phys. Rev. C **64**, 014902 (2001).
[22] D. A. Brown, F. Wang, and P. Danielewicz, Phys. Lett. **B470**, 33 (1999).
[23] D. A. Brown and P. Danielewicz, Phys. Lett. **B398**, 252 (1997).
[24] D. A. Brown, A. Enokizono, M. Heffner, R. Soltz, P. Danielewicz, and S. Pratt, Phys. Rev. C **72**, 054902 (2005).
[25] P. Danielewicz and S. Pratt, Phys. Lett. **B618**, 60 (2005).
[26] J. Applequist, Theor. Chem. Acc. **107**, 103 (2002).
[27] G. F. Bertsch, P. Danielewicz, and M. Herrmann, Phys. Rev. C **49**, 442 (1994).
[28] D. A. Brown and P. Danielewicz, Phys. Rev. C **57**, 2474 (1998).
[29] S. Pratt and S. Petriconi, Phys. Rev. C **68**, 054901 (2003).
[30] Y. Kim, R. T. de Souza, C. K. Gelbke, W. G. Gong, and S. Pratt, Phys. Rev. C **45**, 387 (1992).
[31] B. K. Jennings, D. H. Boal, and J. C. Shillcock, Phys. Rev. C **33**, 1303 (1986).
[32] C. J. Gelderloos *et al.*, Phys. Rev. Lett. **75**, 3082 (1995).
[33] R. Lednicky, V. Lyuboshits, B. Erazmus, and D. Nouais, Phys. Lett. **B373**, 20 (1996).
[34] S. Voloshin, R. Lednicky, S. Panitkin, and N. Xu, Phys. Rev. Lett. **79**, 4766 (1997).
[35] R. Ghetti, J. Helgesson, V. Avdeichikov, B. Jakobsson, N. Colonna, and H. W. Wilschut, Phys. Rev. C **70**, 034601 (2004).
[36] F. Wang and S. Pratt, Phys. Rev. Lett. **83**, 3138 (1999).
[37] F. Retiere and M. A. Lisa, Phys. Rev. C **70**, 044907 (2004).
[38] B. Tomasik, Acta Phys. Pol. B **36**, 2087 (2005).
[39] J. Adams *et al.* (STAR Collaboration), Phys. Rev. Lett. **91**, 262302 (2003).
[40] F. Retiere (STAR Collaboration), Nucl. Phys. **A715**, 591 (2003).
[41] P. Cvitanovic, Phys. Rev. D **14**, 1536 (1976).